Investigation of Pre-Ignition Propellant Mixing in Rotating Detonation Rocket Engine

Quentin Roberts

A thesis
submitted in partial fulfillment of the
requirements for the degree of

Master of Science in Aeronautics and Astronautics

University of Washington
2023

Committee:
Carl Knowlen
James Koch

Program Authorized to Offer Degree:
Aeronautics and Astronautics

University of Washington

Abstract

Investigation of Pre-Ignition Propellant Mixing in Rotating Detonation Rocket Engine

Chair of the Supervisory Committee:
Carl Knowlen
Aeronautics and Astronautics

Pre-ignition propellant mixing was simulated using computational fluid dynamics in various rotating detonation rocket engine (RDRE) configurations. Two different RDREs were used for the simulations, a 25.4 mm diameter RDRE and a 10 mm diameter RDRE. The 25.4 mm diameter RDRE used multiple configurations, with different core plug sizes producing a 3 mm, 5 mm, and 7 mm wide annular combustion chamber, as well as a coreless cylindrical 25.4 mm diameter combustion chamber configuration. The 25.4 mm RDRE used methane and oxygen propellants. The 10 mm diameter RDRE was operated and simulated only in a coreless configuration, but with both methane and oxygen propellants, and hydrogen and oxygen propellants. Four cases for each configuration were simulated, three with similar total mass flow rates and equivalence ratios near stoichiometric, fuel rich, and fuel lean, and the fourth varying total mass flow rate. Mixing was simulated in ANSYS Fluent using a standard $k-\omega$ turbulence model, and a non-reacting species transport model. Simulation results were verified by comparing simulated wall pressure data and injector discharge coefficient data with experimental data. Average mixedness and mixed layer location versus distance from the injector face were compared across the simulated RDREs, propellant combinations, configurations and cases. Frames from high speed video of experimental hot fire tests were compared with simulations, comparing radial mixing trends with radial luminosity profiles.

Contents

List of Figures

List of Tables

Acknowledgements

The author is very appreciative of his research advisor Dr. Carl Knowlen for the opportunity to work in the RDE lab and his assistance with this project, and Ty Mundt and Mitsuru Kurosaka for their many contributions to the research upon which this project is based. In addition, the author thanks the University of Washington student technology fund for funding for the high-speed camera used for this project. The author would also like to thank AFOSR and Jacobs for their financial support of this project through AFOSR Grant FA 9550-18-1-9-0076 with program manager Dr. Chiping Li and Jacobs Technology contract FA 9300-20-F-9801 with program manager Dr. Eric Paulson.

Chapter 1

Introduction

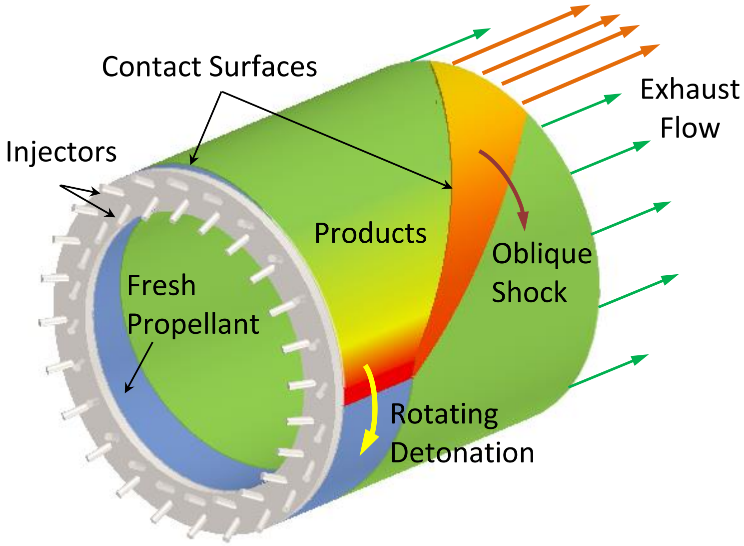

Figure 1.1: Rotating detonation rocket combustor.[1]

A rotating detonation engine (RDE) has propellant flowing axially in an annulus that is combusted with one or more transverse spinning detonation waves [5], [6]. A diagram of the flow through a RDE combustor is shown in figure 1.1. Propellants, a fuel and an oxidizer, are introduced unmixed through injectors and mix in the combustion chamber, producing a layer of fresh propellant. The layer of fresh propellant grows until a detonation passes through it and combusts it, producing hot, high pressure combustion products, which can be accelerated through a nozzle to produce thrust [1].

A detonation wave is a shock wave driven by heat release that generates high pressure and temperature combustion products [7]. This is in contrast to deflagration waves, which are employed by conventional combustors, and are subsonic and produce combustion products at a higher temperature, but lower static pressure immediately behind the deflagration wave [7]. RDEs potentially have higher efficiency than engines utilizing deflagrative combustion due to the near constant volume combustion accomplished by the detonation wave in an RDE [6], [8]. Applications include air-breathing propulsion, terrestrial power generation and rocket engines [9]. When all of the oxidizer and fuel are carried aboard the vehicle and are the only propellants injected into the engine, this propulsion system is often referred to as a Rotating Detonation Rocket Engine (RDRE). Investigations of propellant mixing in RDEs have been performed with both numerical and experimental methods [10], [11], [12], [13].

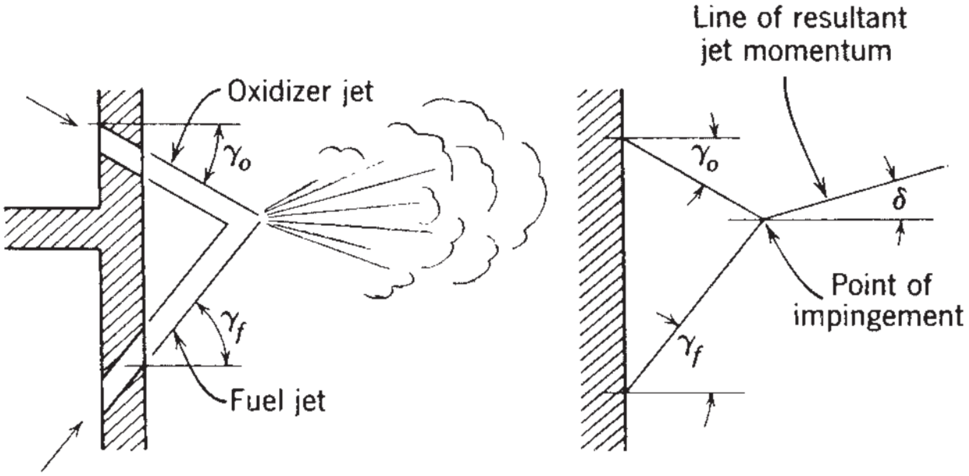

Figure 1.2: Angular relations for an oxidizer-on-fuel impinging doublet injector, adapted from Sutton.[2]

One of the types of injectors used in RDEs is the impinging doublet injector, as shown in figure 1.2. In this type of injector, there is a seperate plenum for the fuel and for the oxidizer. Propellants are fed into the combustion chamber through orifices that are aligned such that the jets of each propellant collide and mix. The direction angle of the momentum of the resulting mixed propellant stream is described by the momentum balance in equation 1.1, a function of the angles of the injector orifices, the mass flow rates of each propellant, $\dot{m}$, and the velocity of each propellant, v [2]. For a given injector design, changes in propellant mass flow rates will change the momentum balance of the impinging doublet, potentially changing the direction and downstream location of the fully mixed propellant layer.

$$tan(\delta) = \frac{\dot{m}_o v_o sin(\gamma_o) - \dot{m}_f v_f sin(\gamma_f)}{\dot{m}_o v_o cos(\gamma_o) + \dot{m}_f v_f cos(\gamma_f)} \tag{1.1}$$

Chapter 2

Background

The effects of annulus size-scale on the operating characteristics on geometrically scaled RDEs are being investigated [3], [14]. In conjunction with this study, the influence of annular gap width in a 25.4-mm RDRE has also been investigated experimentally [4]. To support the experimental investigation, CFD simulations of the injected propellant into the combustor at the gap widths tested has been initiated to gain a better understanding of the flow conditions and degree of mixing prior to ignition. Similar propellant injector studies have been conducted. These include numerical and experimental studies that have investigated radial injection designs and their influence on detonation wave position [13], [15], [16]. Impinging doublet type injector propellant mixing in RDREs and its effect on detonation waves has also been investigated previously , [10], [11]. The experimental hardware and test data are briefly summarized and the numerical procedures and results are presented here.

Chapter 3

Experimental Facility and Procedures

The RDRE test facility has a test stand with a 10-in exhaust duct to which the test RDREs were mounted. The exhaust duct routes combustion products to a large-volume dump tank (4 m^3) that was evacuated as needed to set back pressure for the experiments. The propellant handling system provided metered propellant with maximum 2% uncertainty in equivalence ratio, ϕ, mass flow rate, $\dot{m}_f$, and mass flux, ψ. Sidewall pressure taps in the combustor provided axial time-averaged pressure data. More details of this facility can be found in references [3],[4], [14], [17].

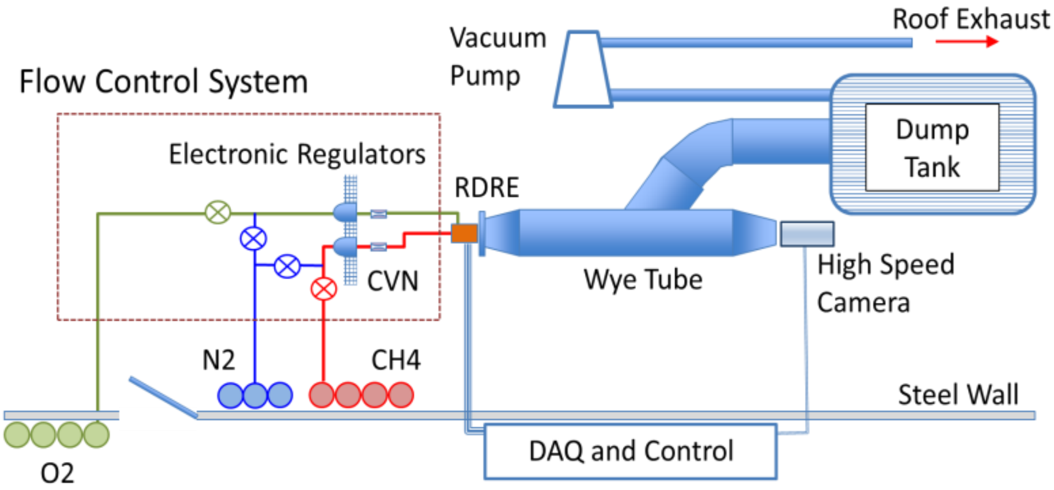

Figure 3.1: Experimental facility layout. [3]

3.1 RDRE Geometry

3.1.1 25.4 mm Engine

Shown in Fig. 3.2 is a section view of the 25.4-mm RDRE used in these experiments. The combustion chamber was made from OFHC copper, with 25.4-mm-diameter by 25.4-mm-long bore forming the outer wall. After the exit of the combustion chamber, the bore expands to 76.2-mm-diameter to match the hole diameter in the mounting flange, which attaches the engine to the exhaust duct. The brass injector sealed the other end of the combustion chamber. An OFHC copper core plug was bolted or threaded to the face of the injector to form the inner wall of the combustion chamber annulus. The 25.4-mm-RDRE was mounted to the test stand that provided oxygen and methane (or hydrogen for some 10 mm RDRE tests) propellant flows at the desired ϕ and ψ.

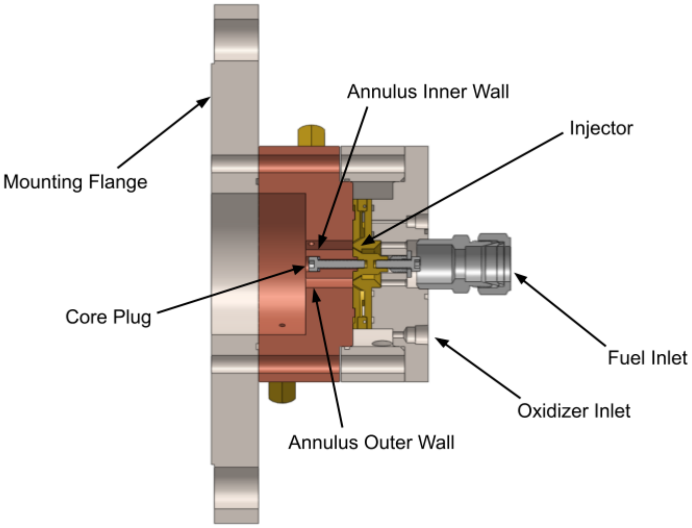

Figure 3.2: Cross-section view of the 25.4 mm RDRE [4].

Different size cores were used to set the annular gap widths as listed in Table 3.1. For the coreless configuration, the core plug was removed and the bolt hole filled with a threaded plug that created a flush injector face surface [4]. The core for the 3-mm-wide annulus configuration had a 42.8° chamfer machined at the injector end to prevent interference with the fuel jet from the injector, as seen in Fig. 3.3.

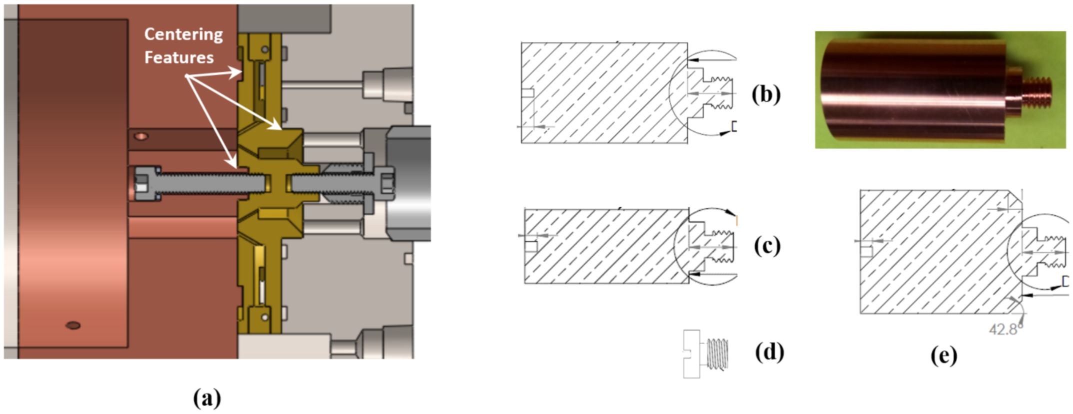

Figure 3.3: a) 25.4 mm RDRE section view. b) Core for 5-mm-gap. c) Core for 7-mm-gap. d) Center plug for coreless configuration. e) Core for 3-mm-gap. [4]

Table 3.1: Combustion chamber annulus dimensions [4].

Annulus OD (mm)	Annulus ID (mm)	Gap Center Dia. (mm)	Gap Width (mm)	Injector/Gap AR
25.4	19.4	22.4	3.0	0.164
25.4	15.4	20.4	5.0	0.108
25.4	11.4	18.4	7.0	0.086
25.4	0	12.7	coreless	0.068

Instrument ports for pressure measurement were drilled at four locations in the combustion chamber sidewall along with one in the 76.2 mm section of the engine. The ports were drilled at varying angles to prevent interference between sensors. Instrument ports were also provided in the fuel and oxidizer plenums. The axial distances of the sidewall ports from the injector face were 17 mm, 19 mm, 20 mm, 22 mm, and 38 mm (last port was in the 76-mm section) [4]. Stand-off tubes having a length-to-diameter ratio of 145 were used with pressure transducers (OMEGA PX319-500A5V). A National Instruments 64-channel data acquisition system was used to sample these sensors at a rate of 2 kHz. Absolute pressure measurement accuracy was $\pm 0.25\%$.

Detonation initiation was achieved with a spark ignited pre-detonator tube using methane and oxygen reactants [14]. It fired radially inwards through a port drilled near the end of the combustion chamber 300 ms after the main propellant valves were opened. Within 200 ms of pre-detonator firing, one of several different steady-state behaviors were typically established. Observed steady-state operating modes were of a single rotating wave without counter-rotating wave, single rotating wave with counter-rotating wave, deflagration without coherent rotating detonation waves, axial pulsations, and quenching.

3.1.2 10 mm RDRE

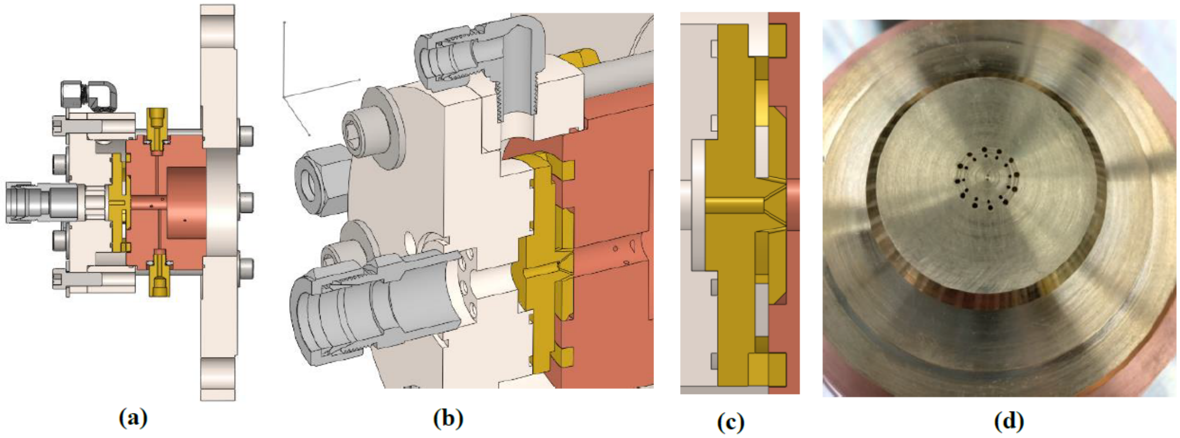

Figure 3.4: 10 mm RDRE geometry. a) Engine cross-section. b) Cross-section isometric view. c) Injector cross-section. d) Photograph of injector face.

Section views of the 10 mm RDRE are shown in figure 3.4. The 10 mm RDRE was a very similar design to the 25.4 mm RDRE. Only the test results from the coreless configuration, with the cylindrical combustion chamber being 10 mm in diameter and 20 mm long, were available at the time of this study. After the combustion chamber section, the bore opened out to a short 51 mm section, and then into the dump tank duct. As in the 25.4 mm RDRE, fuel was fed into the central plenum to feed the injector, and oxidizer fed into the outer plenum. Five 1.57-mm-diameter ports were drilled into the combustion chamber for pressure measurement ranging in distance from the injector face by 9, 11, 13, 15, and 17 mm. Azimuthal angle of the ports was varied to allow for clearance between pressure transducers. An additional 2.38-mm-diameter port was drilled 17 mm from the injector for the pre-detonator ignitor. A sixth 1.57 mm port was drilled 33 mm from the injector in the 51 mm section for backpressure measurement.

3.2 Injector Geometry

3.2.1 25.4 mm RDRE

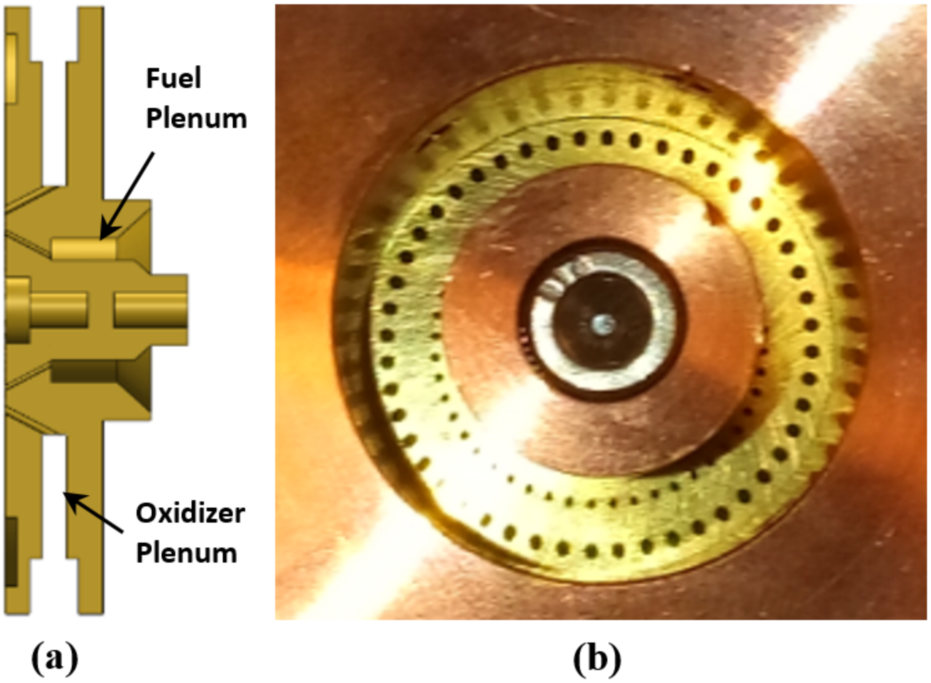

Figure 3.5: 25.4 mm RDRE injector. a) Cross section. b) Photograph of installed injector. [4].

The injector for the 25-mm-combustor was an oxidizer-on-fuel doublet injector with 48 impinging pairs. It was machined from 360 brass. Parameters of the injector design are provided in Table 3.2. Each doublet impinged at an included angle of 60° with the fuel and oxidizer orifices both angled 30° from the central axis. The oxidizer orifice was 0.81 mm in diameter and the fuel orifice was 0.51 mm in diameter, resulting in an oxidizer-to-fuel orifice area ratio of 2.56. The radius from the center of the combustion chamber to the impingement point was 10.2 mm, which corresponds to the center of the 5-mm-wide annular gap configuration. All the fuel orifices were fed from a coaxial annular plenum, and all the oxidizer orifices were fed from a radial plenum, as seen in Fig. 3.5. Centering features were designed into the injector to center the core inside the outer wall of the combustion chamber. Discharge coefficients under cold flow conditions were

0.73 for the oxidizer orifices, and 0.75 for the fuel orifices.

Table 3.2: 25.4 mm Engine Injector dimensions and characteristics [4].

Number of Pairs =	48	Impingement Angle =	60°
Oxidizer d (mm) =	0.81	Impingement d (mm) =	20.4
Fuel d (mm) =	0.51	Oxidizer/Fuel AR =	2.56
Ox. Angle From Axis =	30°	Oxidizer C_d =	0.73
Fuel Angle From Axis =	30°	Fuel C_d =	0.75

3.2.2 10 mm RDRE

The injector for the 10 mm RDRE is shown in figure 3.4c and 3.4d. It is of a similar oxidizer-on-fuel impinging doublet design to the 25.4 mm RDRE and machined from 360 brass. The injector used the same orifice diameters, 0.81 mm for oxidizer and 0.51 mm for fuel, as the injector for the 25.4 mm RDRE. In contrast to the injector for the 25.4 mm RDRE, the 10 mm RDRE injector used only 12 impinging pairs, and an oxidizer port inclination of $11.3°$ in order for the injector momentum balance to be axial at a fuel equivalence ratio of 1.15. Also, a cylindrical fuel plenum was used instead of the annular plenum in the 25.4 mm RDRE. Discharge coefficients observed during the experiment for oxygen/methane experiments were 0.78 for the oxidizer and 0.80 for the fuel. A discharge coefficient of 0.76 was observed for hydrogen during oxygen/hydrogen experiments.

Table 3.3: 10 mm Engine Injector dimensions and characteristics.

Number of Pairs =	12	Impingement d (mm) =	8.5
Oxidizer d (mm) =	0.81	Oxidizer/Fuel AR =	2.56
Fuel d (mm) =	0.51	Oxidizer C_d =	0.78
Ox. Angle From Axis =	11.3°	Methane C_d =	0.80
Fuel Angle From Axis =	30°	Hydrogen C_d =	0.76
Impingement Angle =	41.3°		

3.3 Experimental Testing and Simulation Cases

3.3.1 25.4 mm RDRE

Experimental testing was conducted over a test matrix that swept both ϕ and ψ. The test matrix covered a sweep over the range 80 kg/s/m^2 $< \psi <$ 400 kg/s/m^2 with constant $\phi \approx 1.15$, and a sweep of the range $0.26 < \phi < 2.6$ with constant $\psi \approx 240$ kg/s/m^2. During testing, the cores for the annular configurations eventually became heavily eroded or burned up. Thus, testing was conducted across as much of the test matrix as possible until core degradation occurred. The test conditions in which the pre-detonator ignitor fired in this investigation are shown in Fig. 3.6, with different plotting symbols indicating the resulting combustor operating mode at each test condition. Data from cold flow situations that resulted when the ignitor did not fire (not shown in Fig. 3.6) were useful for comparing the results of propellant injection simulations without chemical reactions.

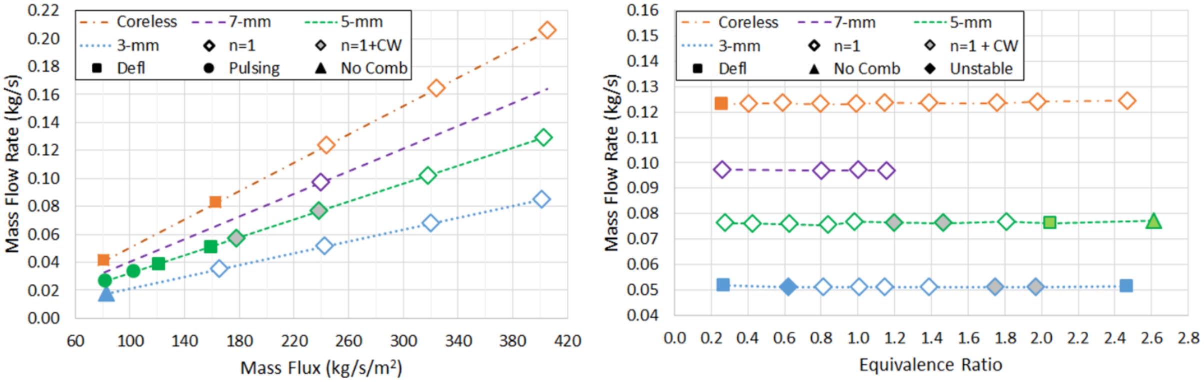

(a) **(b)**

Figure 3.6: Mass flow rate data from hot fire tests with different engine configurations. a) ψ sweep at constant $\phi = 1.15$. b) ϕ sweep at constant $\psi = 240 kg/s/m^2$. [4]

For the simulation test conditions, an effort was made to examine the range of conditions explored in the experiments. Only cold flow tests were of interest for these simulations to enable comparison of plenum and sidewall pressure data. Because cold flow tests were not carried out at all test conditions, simulations were not conducted at exactly the same conditions for each configuration. For some configurations, no cold flow tests were available, and hot fire test conditions were substituted. All simulation cases were selected to replicate conditions for either and experimental cold flow or hot fire. The simulation test cases listed in Table 3.4 were selected for the constant ψ sweep with simulations at or near $\phi = 1.15$, $\phi = 1.8$, and $\phi = 0.6$ with constant ψ, as well as the constant ϕ sweep with one simulation at or near $\phi = 1.15$ with a ψ significantly higher or lower than the center of the test matrix.

Table 3.4: 25.4 mm RDRE simulation case matrix

Engine Config.	Run Number	ϕ	ψ (kg/s/m^2)	$w_{f,opt}$	$\dot{m}$ (g/s)	Backpressure (kPa)
3 mm	304	0.63	239	0.136	50.49	-48.3
	288	1.18	240	0.228	50.75	-99.0
	291	1.8	242	0.310	51.09	-48.3
	319	1.21	498	0.232	105.19	-99.3
5 mm	408	0.63	159	0.136	50.95	-50.3
	216	1.18	178	0.228	57.08	-99.0
	192	2.63	242	0.397	77.59	-48.3
	234	1.16	139	0.225	44.70	-99.3
7 mm	338	0.27	237	0.0632	95.72	-48.3
	342	0.42	236	0.0950	95.34	-49.0
	337	1.03	239	0.205	96.54	-48.3
	334	1.20	172	0.231	96.45	-46.2
coreless	129	0.41	242	0.0930	122.41	-48.3
	69	1.13	172	0.220	87.28	-99.3
	89	1.81	242	0.312	122.46	-43.4
	93	1.18	504	0.228	203.93	-42.1

3.3.2 10 mm RDRE

Experimental testing for the 10 mm RDRE was carried out over a test matrix sweeping both ϕ and ψ for oxygen-methane and oxygen-hydrogen propellant combinations. For both propellant combinations, mass flux sweeps were carried out between out 80 kg/s/m^2 and 300 kg/s/m^2 and a constant $\phi \approx 1.15$. A ϕ sweep at constant $\psi = 243$ kg/s/m^2 between $\phi \approx 0.8$ and $\phi \approx 1.5$ for methane was also carried out, and for hydrogen, a ϕ sweep at constant $\psi = 187$ kg/s/m^2 between $\phi \approx 0.3$ and $\phi \approx 1.4$. Operating modes for these test matrices are plotted in figure 3.7.

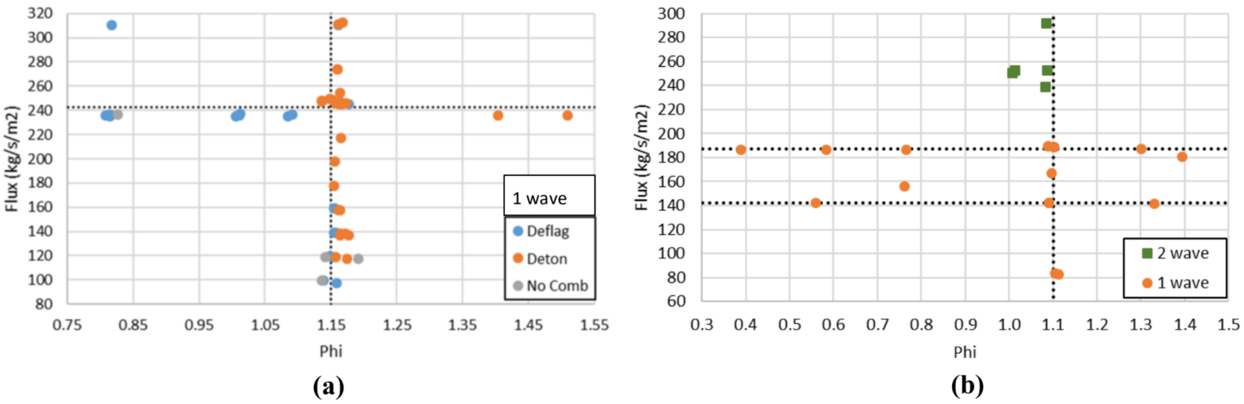

Figure 3.7: 10 mm RDRE operating modes. a) CH_4/O_2 b) H_2/O_2

Using the same methodology as for the 25.4 mm RDRE, simulation cases were selected from the experimental cold flow and hot fire test matrix. For methane, three simulations sweeping ϕ were conducted, with a fourth at near-stoichiometric ϕ but at a lower mass flux. For hydrogen, four simulations sweeping ϕ at constant mass flux were conducted, with a fifth at higher mass flux. Simulation cases for the 10 mm RDRE are listed in table 3.5.

Table 3.5: 10 mm RDRE simulation case matrix

Propellants	Run Number	ϕ	ψ (kg/s/m^2)	$w_{f,opt}$	$\dot{m}$ (g/s)	Backpressure (kPa)
CH_4/O_2	50	0.83	236	0.172	18.56	-50.3
	172	1.12	248	0.218	19.40	-50.3
	148	1.75	243	0.304	19.10	-48.2
	84	1.14	119	0.222	9.33	-99.2
H_2/O_2	31	0.39	186	0.0463	14.62	-50.3
	32	0.58	187	0.0680	14.67	-50.3
	33	0.77	187	0.0875	14.67	-50.3
	30	1.39	181	0.148	14.18	-50.3
	17	1.01	253	0.112	19.85	-50.3

Chapter 4

Numerical Methods

The CFD simulations model the injection of gaseous methane or hydrogen and oxygen through an injector having the key geometric features of the experimental apparatus. The flow structures are tracked and the molecular mixing of propellants is quantified throughout the computational domain. The definition of of mixedness used here is provided in the following section and the details of the numerical method are then presented. The results discussed here of a mesh refinement study using the mixedness parameter were used to establish grid coarseness to be used throughout this investigation.

4.1 Definition of Mixedness

Mixedness was a parameter used to quantify how close the two propellants were to being mixed at a ratio of $w_{f,opt}$, which is the desired methane mass fraction for a given simulation case. Mixedness equals one when the $w_{f,opt}$ is reached and is less than one when the mixture is not at the $w_{f,opt}$. A mixture with a methane mass fraction of one by the provided definition has a mixedness of zero, and a mixture with a methane mass fraction equal to zero has a varying mixedness depending on what $w_{f,opt}$ is, as seen in Fig. 4.1. Mixedness is defined in Eq. 4.1. ϕ is the fuel equivalence ratio, the ratio between stoichiometric oxidizer-to-fuel mass ratio, $({}^{O}\!/\!{}_{F})_{stoich.}$, to the actual oxidizer-to-fuel mass ratio, $({}^{O}\!/\!{}_{F})$. For methane and oxygen, $({}^{O}\!/\!{}_{F})_{stoich.} = 4$, and for hydrogen and oxygen,

$({}^{O}\!/{}_{F})_{stoich.} = 8$. The relationship between ϕ and w_f for a fuel/oxidizer combination with no other species present is defined in Eq. 4.2.

$$\xi = 1 - \sqrt{(w_f - w_{f,opt})^2/(1 - w_{f,opt})^2} \tag{4.1}$$

$$\phi = \frac{({}^{O}\!/{}_{F})_{stoich.}}{({}^{O}\!/{}_{F})} = \frac{({}^{O}\!/{}_{F})_{stoich.} w_f}{w_o} = \frac{({}^{O}\!/{}_{F})_{stoich.} w_f}{1 - w_f} \tag{4.2}$$

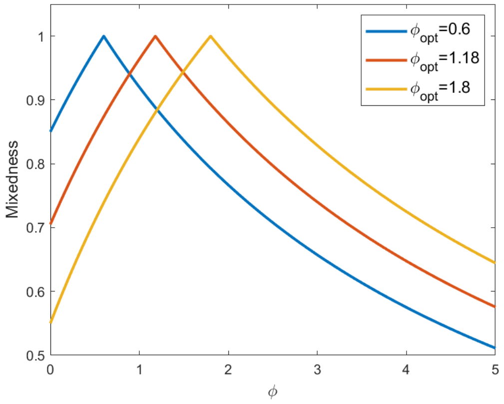

Figure 4.1: ϕ vs. mixedness plotted for oxygen and methane propellants and three different optimum values of ϕ.

Under the flow conditions observed in the simulations, some areas have a high mixedness, but a low mass flux. To prevent these areas from skewing the quantification of propellant mixedness, mixedness values were weighted by mass flux. To weight the values of mixedness, the axial mass flux for each cell center of each transverse x plane was computed, and then normalized by the minimum and maximum mass flux values for that plane, producing a weight value between 0 and 1 for each cell. The mixedness for each cell was then multiplied by this weight value. The resulting value is referred to as mass flux weighted mixedness. Mass flux weighted mixedness is reported both averaged versus radius over transverse planes at varying distance from the injector to examine radial mixing dependence, and averaged over entire transverse x planes to examine axial mixing dependence.

4.2 Solver

The simulations in this study were performed using ANSYS Fluent [18]. Turbulence was simulated using the standard two equation $k-\omega$ model with shear flow corrections and production limiter options and mixing was simulated using a non-reacting species transport model with diffusion energy source option [19]. Three gases were modeled in the domain, oxygen, methane, and nitrogen. For simulations utilizing hydrogen fuel, methane was replaced with hydrogen. Most simulations were initialized with hybrid initialization, but this produced instabilities with some simulations, so the initial conditions for these simulations were modified to eliminate initial non-axial velocity. The simulations were initially converged in steady state using first order upwind spatial discretization, and then converged again using second order upwind. Steady state convergence, as indicated by residuals ceasing to monotonically decrease, was not always attained with all residuals being less than 10^{-4}, so the simulations were switched to transient after steady state convergence and five time steps of $2 * 10^{-8}$ s were simulated to attain convergence at lower residuals. For steady state simulations, pseudo transient with a pseudo transient time scale factor of 1 was used. For transient simulations, second order upwind spatial discretization, first order implicit transient formulation, and a flow Courant number of 0.9 were used.

4.3 Domain and Mesh

To reduce computational cost the fluid domain was split in half axially by a symmetry plane for the 25.4 mm annular configurations as shown Fig. 4.2a, and one fourth symmetry was used for the 25.4 mm coreless configuration. Due to its smaller size, the full domain for the 10 mm RDRE was modeled, as shown in figure 4.3. Both plenums were modeled as part of the simulation domain. Inlet mass flow boundary conditions were specified at the inlets of the plenums, with the mass fraction of methane or hydrogen and oxygen set to unity at the inlets of their respective plenums. The outlet of the domain was a pressure outlet boundary condition with pure nitrogen reverse flow to account for possible back flow from the dump tank that was distinct from the fuel and oxidizer gases. No-slip wall boundary conditions were used for all the solid walls of the domain.

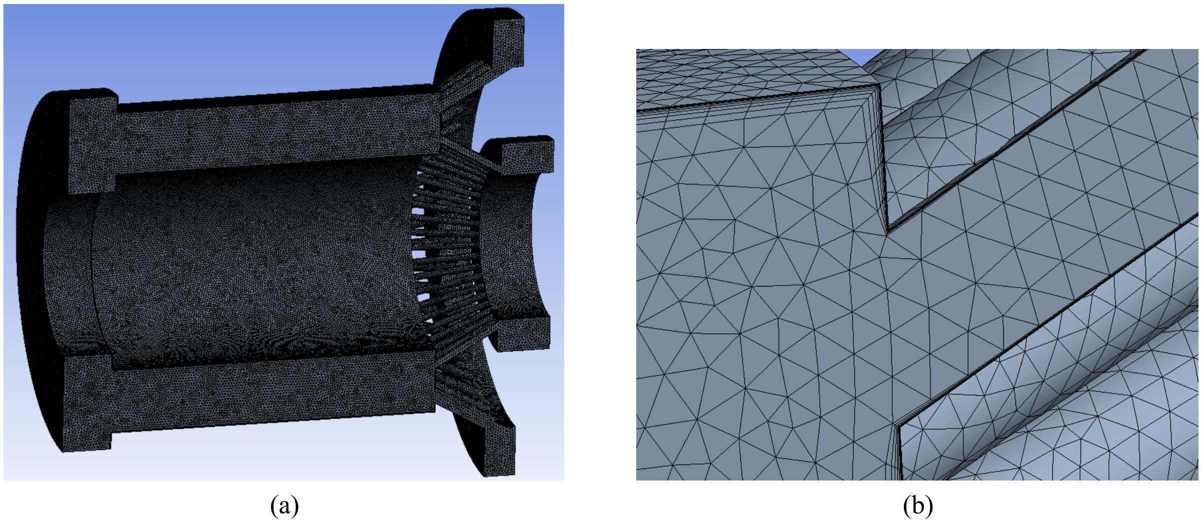
(a) (b)

Figure 4.2: Meshes used for 25.4 mm RDRE in 5 mm wide annular configuration simulations. a) Full mesh. b) Magnified view of injector region.

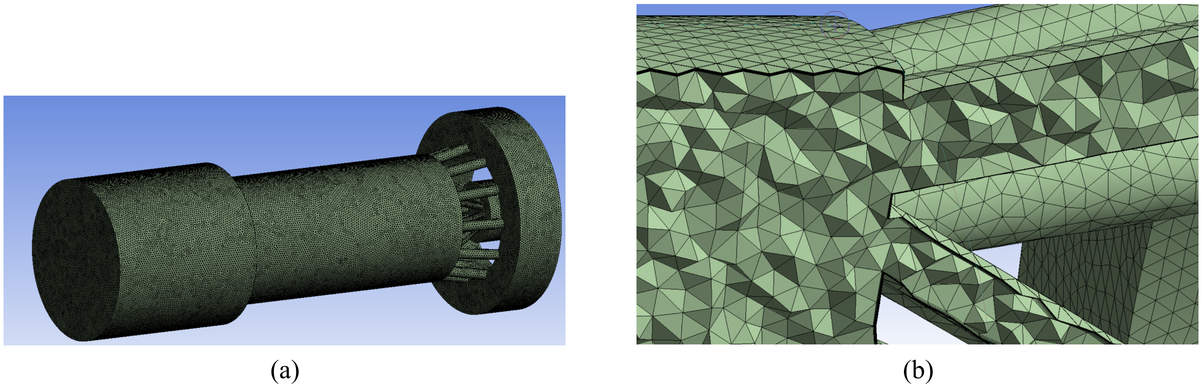
(a) (b)

Figure 4.3: Meshes used for 10 mm RDRE simulations. a) Full mesh. b) Magnified view of injector region.

The mesh for this study was an unstructured tetrahedral mesh with wedge elements forming the inflation layer at the walls to capture the boundary layer flow (Fig. 4.2b). Boundary layer inflation was specified to be 10 layers with a growth rate of 1.4, with the first layer height calculated to be at approximately $y_+ = 5$ per the recommendation of Rodriguez for the $k - \omega$ turbulence model [20]. A mesh convergence study was performed using the mesh for the coreless 25.4 mm engine configuration. The five mesh resolutions listed in Table 4.1 were considered. The four coarsest mesh resolutions utilized the one-fourth symmetry mesh, while the finest resolution was forced to utilize a one-eighth symmetry mesh due to computational limitations. Each mesh was used to simulate the pre-combustion flow field for $\phi = 1.13$ and $\psi = 172$ kg/s/m^2. Wall pressure data for each mesh resolution was compared with experimental non-combustion data to judge accuracy in relation to the experiment. The mass-weighted average and standard deviation of methane mass fraction at multiple planes at varying distance from the injector were compared across each mesh resolution to monitor convergence of the species mixing aspect of the flow field.

Table 4.1: Mesh resolutions for coreless mesh resolution study.

Element Count (Million)	Global Element Size (mm)
1.6	0.40
3.2	0.25
6.0	0.20
13.6	0.15
13.4 With 1/8 Symmetry	0.12

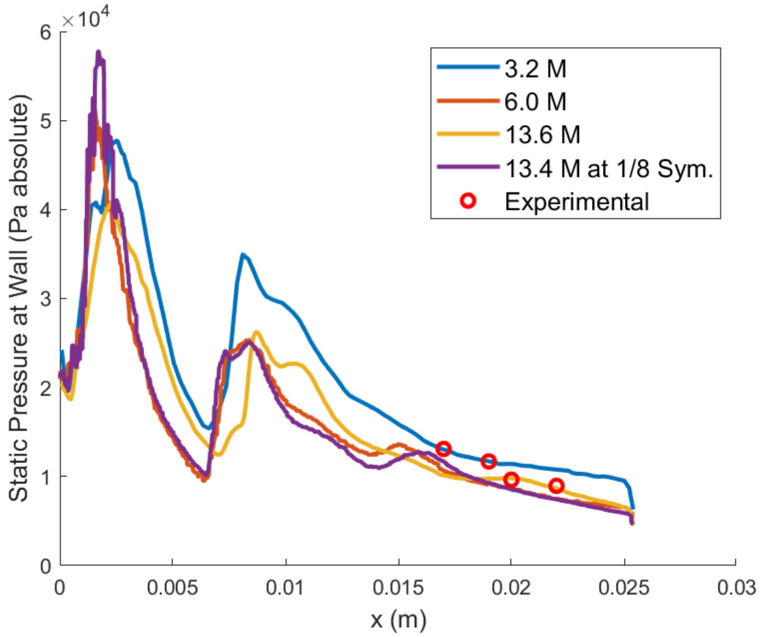

Figure 4.4: Wall pressures at different mesh resolutions compared with experimental data.

The mesh resolutions did not significantly affect the shapes of the wall pressure distributions.

All mesh resolutions finer than 6 million elements did not produce more accurate wall pressure values compared to experiment, as seen in Fig. 4.4. Thus, based on pressure, the 6 million element mesh provided reasonable answers for less computational cost than the finer meshes.

Comparing the contours of methane mass fraction at the $x = 10$ mm plane in Fig. 4.5, the 1.6 million element mesh does not produce the same interwoven tendril-like flow structure as the simulations with finer meshes. The 3.2 million element mesh resolves this structure more than the 1.6 million, but not as much as the 6 million element or finer meshes. The 6 million element mesh simulation produces a similar flow field to that with the 13.6 million element mesh, but with some of the tendrils of methane still merging together like in the 3.2 million element mesh simulation. Using the 13.6 million element mesh, the tendrils of methane are almost entirely separated by layers of oxygen. The 13.6 million element mesh was considered to be fine enough to produce a converged methane mass fraction flow field, with the 13.4 million element one-eight symmetry mesh producing a nearly identical flow field.

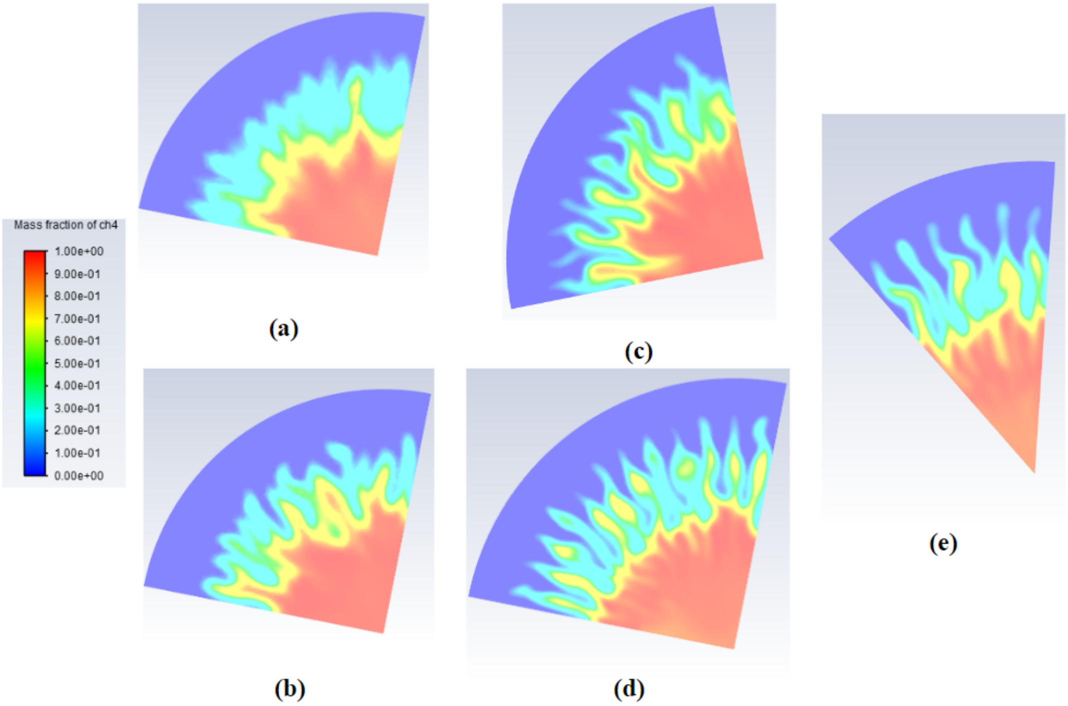

(a) **(c)** **(e)** **(b)** **(d)**

Figure 4.5: Contours of w_f at $x = 10$ mm from the injector face. a) 1.6 million element. b) 3.2 million element. c) 6.0 million element. d) 13.6 million element. e) 13.4 million element with $^1/_8$ symmetry.

Based on the metrics presented here, the 6 million element mesh resolution was selected for the simulations in this study. It was selected because it had similar wall pressure accuracy as the other mesh resolutions, produced very similar bulk mixing results to the finer meshes, and had the second-best resolved methane contours, as well not being as computationally expensive as the extra fine mesh resolution. A direct comparison of bulk mixing attributes between the 6 million element mesh and the finest mesh tested is shown in figures 4.6 and 4.7.

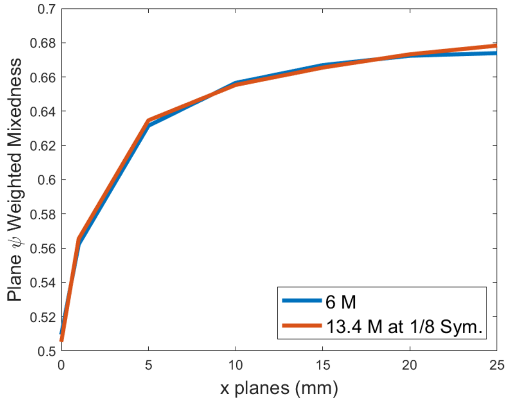

Figure 4.6: Comparison of plane averaged mixing distribution between 6 million element and 13.4 million element $^1/_8$ symmetry mesh resolutions.

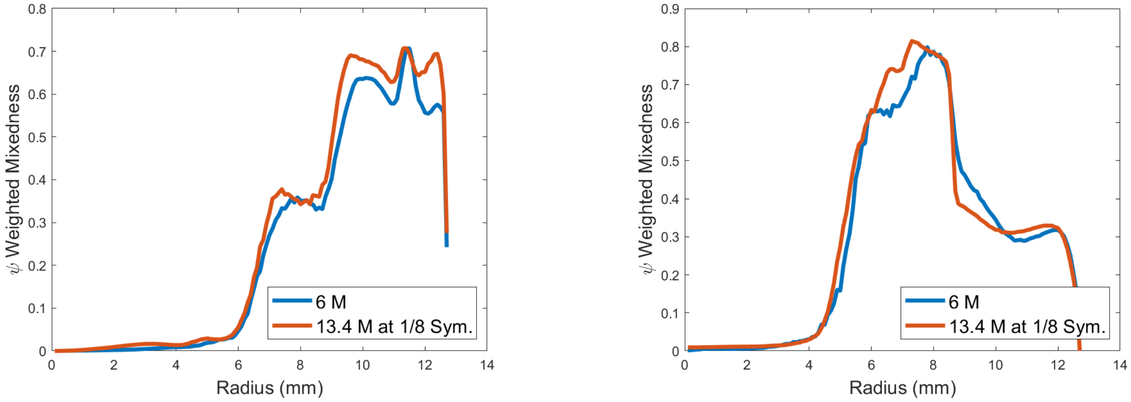

(a) (b)

Figure 4.7: Comparison of radial mixing distribution between 6 million element and 13.4 million element $^1/_8$ symmetry mesh resolutions at two different distances from the injector face, x. a) $x = 10$ mm. b) $x = 25$ mm.

Chapter 5

Computational Results and Discussion

5.1 Wall Pressure Data

Static pressure data along the outer wall of the combustion chamber along a line at the center plane of an injector pair and along a line at the plane midway between two injector pairs were collected for all simulations. For test runs where there was non-combustion pressure data available, the wall pressure data from the simulations was compared with experimental data. Simulated and experimental wall pressure data for the 25.4 mm RDRE coreless and 5-mm-gap configurations are plotted together for two representative simulations in figure 5.1, showing that simulated wall pressure data compares well with experimental results for both the pressure amplitudes and sign of the pressure gradients. Simulated pressure amplitude was within 16% of experimental.

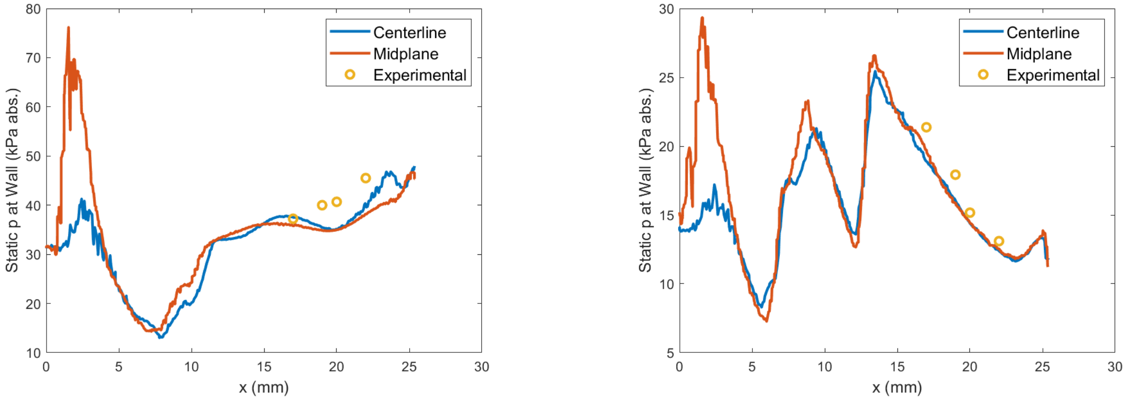

(a)

(b)

Figure 5.1: 25.4 mm RDRE simulated wall pressures at injector center plane and midplane between injector pairs plotted with experimental data. a) Coreless configuration $\phi = 1.13$, $\psi = 172$ kg/s/m^2. b) 5 mm annular configuration, $\phi = 1.18$, $\psi = 216$ kg/s/m^2.

Similarly, for the 10 mm RDRE, static wall pressures were recorded from the simulation and compared with experimental values. Representative plots of static wall pressures are shown for the 10 mm RDRE using both oxygen-methane propellant (figure 5.2), and oxygen-hydrogen propellant (figure 5.3). Pressure amplitudes compare well between the simulated and experimental pressure data, and pressure gradient sign compared relatively well with some cases closer than others. Simulated pressure amplitude was within 26% of experimental. Comparing pressure data directly to experimental values in this way provided a point of reference for verification of the numerical models used in this study.

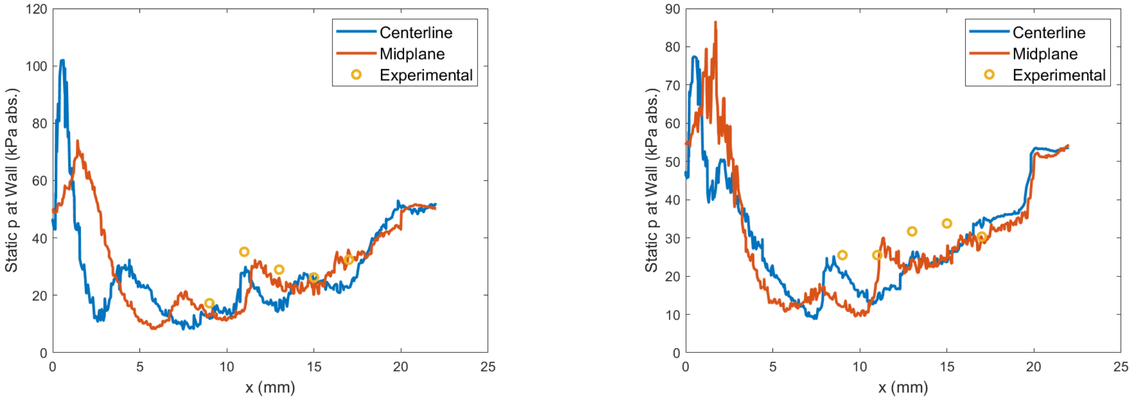

(a) (b)

Figure 5.2: Simulated wall pressures at injector center plane and midplane between injector pairs plotted with experimental data for 10 mm RDRE with oxygen-methane propellant. a) $\phi = 0.83$, $\psi = 236\ \text{kg/s/m}^2$. b) $\phi = 1.75$, $\psi = 243\ \text{kg/s/m}^2$.

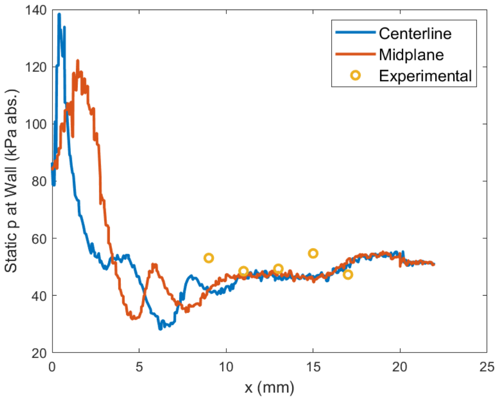

Figure 5.3: Simulated wall pressures at injector center plane and midplane between injector pairs plotted with experimental data for 10 mm RDRE with oxygen-methane propellant, $\phi = 1.01$, $\psi = 253\ \text{kg/s/m}^2$.

5.2 Discharge Coefficients

As another point of comparison between the numerical models and experimental data, steady-state static plenum pressures were obtained from the numerical simulations. From these plenum pressures, discharge coefficients were calculated and the average compared with the average observed discharge coefficients from experimental testing. Flow through the injector orifices was found to be choked in all test conditions examined. Choked flow was ascertained from the ratio observed between the injector plenums pressure, p_0 and pressure at the orifice exit, p^*, which was higher than the required pressure ratio for choked flow found from equation 5.1, and by examination of simulated Mach number contours, as seen in figure 5.4 [21]. Given choked flow conditions, the ideal mass flow rate through the orifice was calculated using equation 5.2, assuming ideal gas, isentropic, one-dimensional flow [21]. From the ideal mass flow rate, the discharge coefficient was found from equation 5.3, the ratio between actual and ideal mass flow rate.

$$\frac{p^*}{p_0} = \left(\frac{2}{\gamma+1}\right)^{\frac{\gamma}{\gamma-1}} \tag{5.1}$$

$$\dot{m}_{ideal} = A^* p_0 \sqrt{\frac{\gamma}{RT_0}} \left(\frac{2}{\gamma+1}\right)^{\frac{\gamma+1}{2(\gamma-1)}} \tag{5.2}$$

$$C_d = \frac{\dot{m}_{actual}}{\dot{m}_{ideal}} \tag{5.3}$$

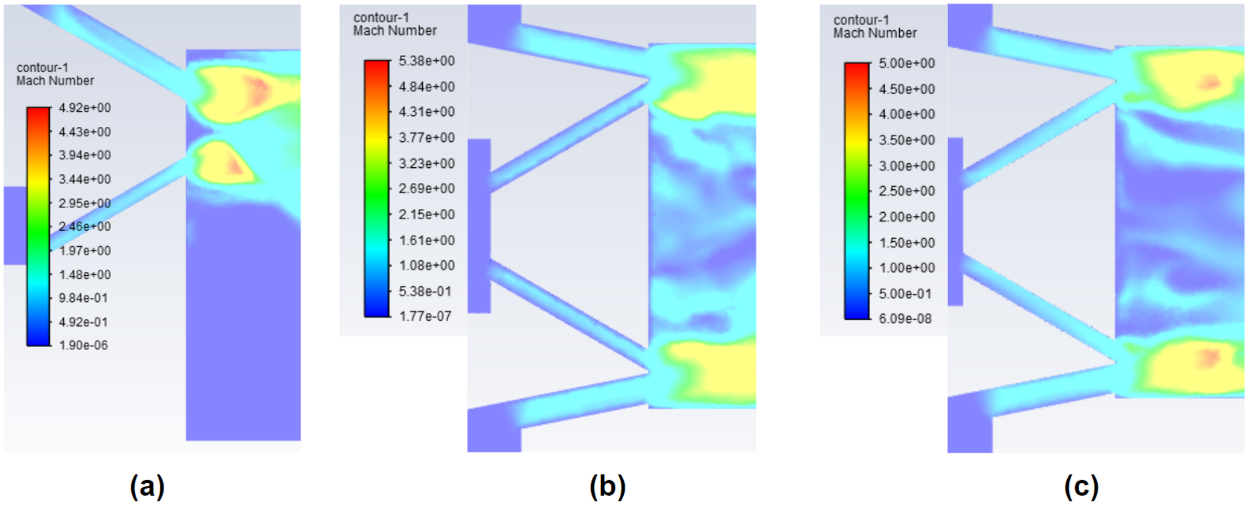

Figure 5.4: Representative simulated Mach number contours plotted on the injector center plane showing choked Mach 1 flow through injector orifices. a) 25.4 mm RDRE coreless confiuration, $\phi = 1.13$, $\psi = 172$ kg/s/m^2. b) 10 mm RDRE, oxygen-methane propellant, $\phi = 1.14$, $\psi = 119$ kg/s/m^2. c) 10 mm RDRE, oxygen-hydrogen propellant, $\phi = 0.40$, $\psi = 186$ kg/s/m^2.

Discharge coefficients for the 25.4 mm RDRE, shown in table 5.1, were found for the both the fuel and oxidizer orifices of the injector. The averages for each orifice across all simulation cases are shown and compared with experimental discharge coefficients obtained from cold flow and hot fire tests. Discharge coefficients for both orifices were consistent across multiple simulation cases, with relatively low standard deviations for each orifice. Comparing with the experimentally derived discharge coefficient, the simulated oxidizer orifice C_D was 2.5 standard deviations larger than experimental, and the fuel orifice C_D was 1.9 standard deviations smaller than experimental.

Table 5.1: Simulated injector discharge coefficient results for 25.4 mm RDRE

Engine Config.	Run Number	Ox. C_D	Fuel C_D
3 mm	304	0.792	0.670
	288	0.796	0.695
	291	0.771	0.698
	319	0.784	0.703
5 mm	408	0.788	0.667
	216	0.754	0.699
	192	0.774	0.730
	234	0.764	0.699
7 mm	338	0.787	0.699
	342	0.795	0.712
	337	0.852	0.770
	334	0.796	0.704
coreless	129	0.790	0.655
	69	0.788	0.700
	89	0.777	0.707
	93	0.769	0.715
	Average:	0.786	0.701
	Standard Deviation:	0.022	0.026
	Experimental:	0.73	0.75

Similarly, for the 10 mm RDRE, simulated discharge coefficient results were consistent, with relatively low standard deviations. Changing fuel from methane to hydrogen did not affect oxidizer C_D, with only a 0.2% difference between the simulated C_D for oxygen-methane and for oxygen-hydrogen propellant. Comparing simulated fuel orifice discharge coefficients between methane and hydrogen, the oxygen-hydrogen propellant had a much lower C_D than the methane, 0.68 versus 0.73. Both sets of simulations underestimated fuel C_D, with the methane simulations underestimating by 9.4 standard deviations, and the hydrogen by 7.5 standard deviations.

Table 5.2: Simulated injector discharge coefficient results for 10 mm RDRE

Propellants	Run Number	Ox. C_D	Fuel C_D
CH_4/O_2	50	0.800	0.731
	172	0.804	0.726
	148	0.940	0.743
	84	0.803	0.734
	Average:	0.834	0.734
	Standard Deviation:	0.058	0.007
	Experimental:	0.78	0.80
H_2/O_2	31	0.809	0.679
	32	0.838	0.692
	33	0.813	0.679
	30	0.776	0.678
	17	0.924	0.662
	Average:	0.832	0.678
	Standard Deviation:	0.056	0.011
	Experimental:	0.78	0.76

5.3 Fuel Mass Fraction Contour Plots

5.3.1 25.4 mm RDRE

Simulation results of methane mass fraction were reported in ANSYS fluent as contours of methane mass fraction on an axial plane bisecting the center-line of an injector pair near the center of the computational domain. The contours for simulations near the center of the test matrix for each engine configuration are shown in Fig. 5.5. For these simulations, $w_{f,opt} \approx 0.23$. Correspondingly, the fully mixed region is colored light blue. It is evident that the spreading of the mixed region in the annulus is a challenge under cold flow conditions. The mixedness in the 5-mm-gap spans the annulus more than in the other configurations. Whereas the mixing in the 3-mm-gap occurs along a thin region next to the inner core surface. The uniformity of the mixedness in the annulus may play a role in how easy the propellant is to ignite, which is a topic still under investigation.

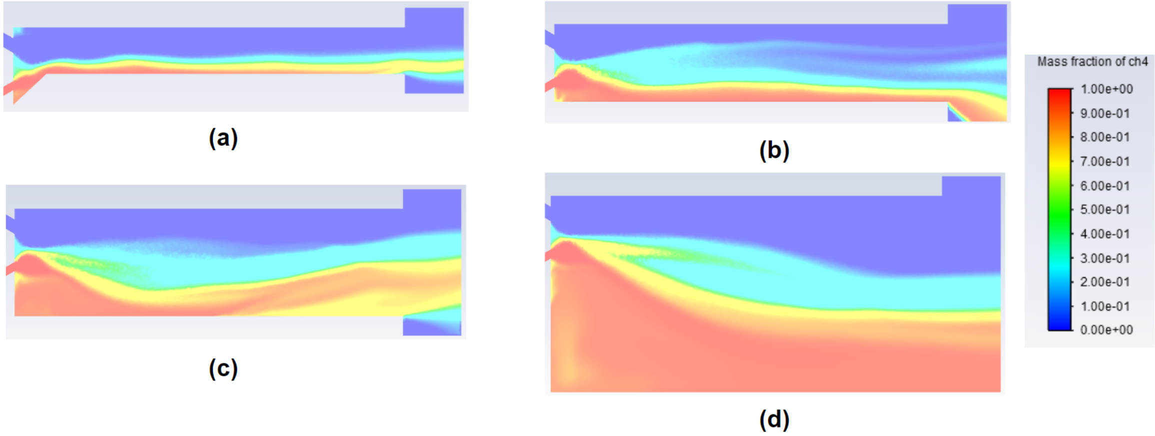

Figure 5.5: 25.4 mm RDRE simulated contours of w_f at injector center plane for near stoichiometric test condition runs. a) 3 mm annular, $\phi = 1.18$, $\psi = 288$ kg/s/m^2. b) 5 mm annular, $\phi = 1.18$, $\psi = 216$ kg/s/m^2. c) 7 mm annular, $\phi = 1.20$, $\psi = 238$ kg/s/m^2. d) Coreless, $\phi = 1.13$, $\psi = 172$ kg/s/m^2.

By plotting velocity vectors on the injector center plane colored by methane mass fraction as in figure 5.6, the flow directions of each propellant as they mix can be visualized. The 5 mm annular configuration, for which the injector pairs were designed to be centered in, produced the fewest eddies at the injector face. The 7 mm annular and coreless configurations, comparatively, had a large recirculating region of methane near the the center of the injector face. In the 3 mm annular configuration, which required a chamfered core to achieve the 3 mm gap size without covering the injector, the methane flow was redirected by the chamfered core into the oxidizer stream.

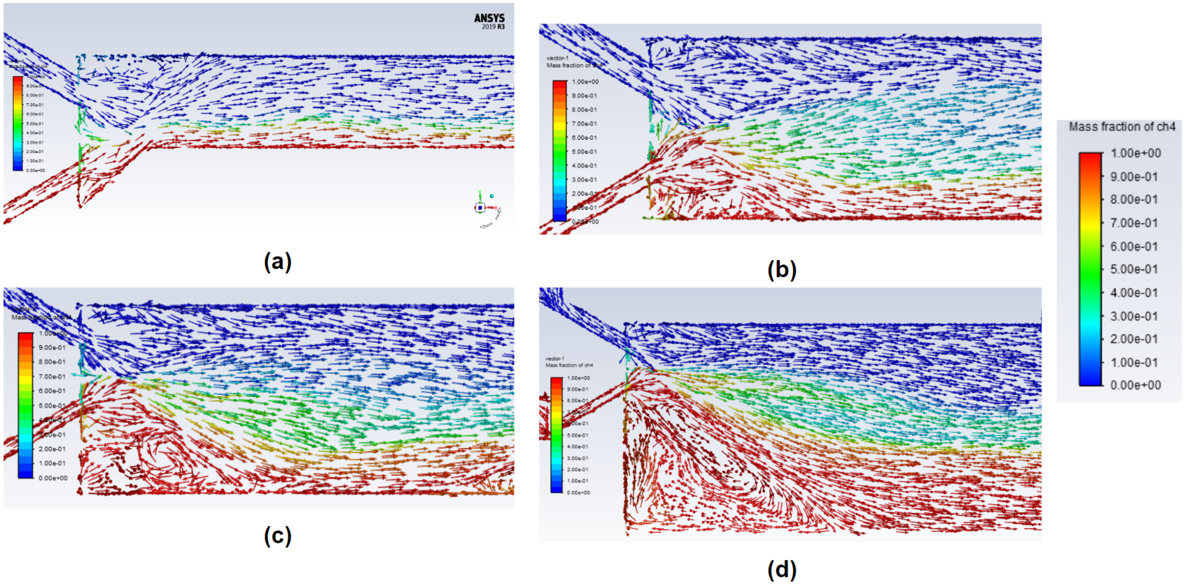

(a)

(b)

(c)

(d)

Figure 5.6: 25.4 mm RDRE simulated velocity direction vectors colored by w_f at injector center plane for near stoichiometric test condition runs. a) 3 mm annular, $\phi = 1.18$, $\psi = 288$ kg/s/m^2. b) 5 mm annular, $\phi = 1.18$, $\psi = 216$ kg/s/m^2. c) 7 mm annular, $\phi = 1.20$, $\psi = 238$ kg/s/m^2. d) Coreless, $\phi = 1.13$, $\psi = 172$ kg/s/m^2.

Another means of displaying the mixing process is to plot contours of fuel mass fraction as shown in Fig. 5.7. The injectors are shown on the right and flow is expanding to the left through an annular combustor with a 5-mm-gap. Planes located at 5 mm increments from the injector show the evolution of the three dimensional flow field. The mixing in between the injector planes is seen to proceed in a similar manner throughout.

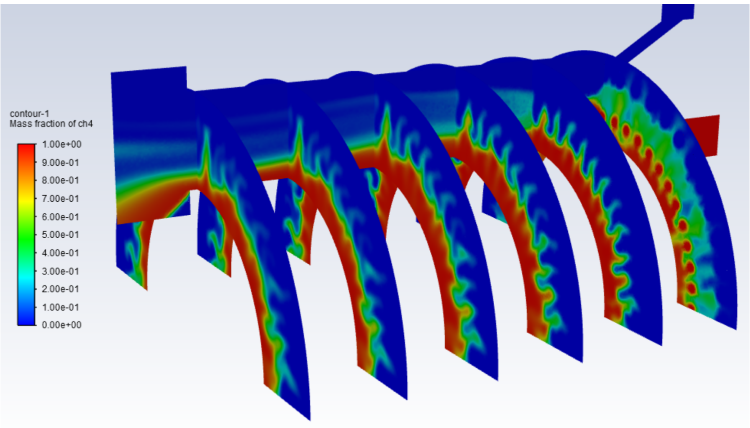

Figure 5.7: 25.4 mm RDRE simulated contours of w_f plotted over injector center plane and transverse planes at $x = 5$ mm, 10 mm, 15 mm, 20 mm, and 25 mm for 5-mm-wide annular configuration, $\phi = 1.18$, $\psi = 216$ kg/s/m^2.

To provide a means of comparison with the simulations for the 10 mm coreless RDRE, the methane mass fraction contours for all four 25.4 mm RDRE simulations are shown in figure 5.8. Qualitatively, ϕ is seen to have a large effect on the injector momentum balance, with higher ϕ conditions resulting in a mixed layer being directed much more towards the outer wall as opposed to towards the center axis of the combustion chamber. ψ is also seen to have a relatively small effect on propellant mixing, with the methane mass fraction contours for similar ϕ but different ψ simulations in figures 5.8b and 5.8d having nearly identical contour plots.

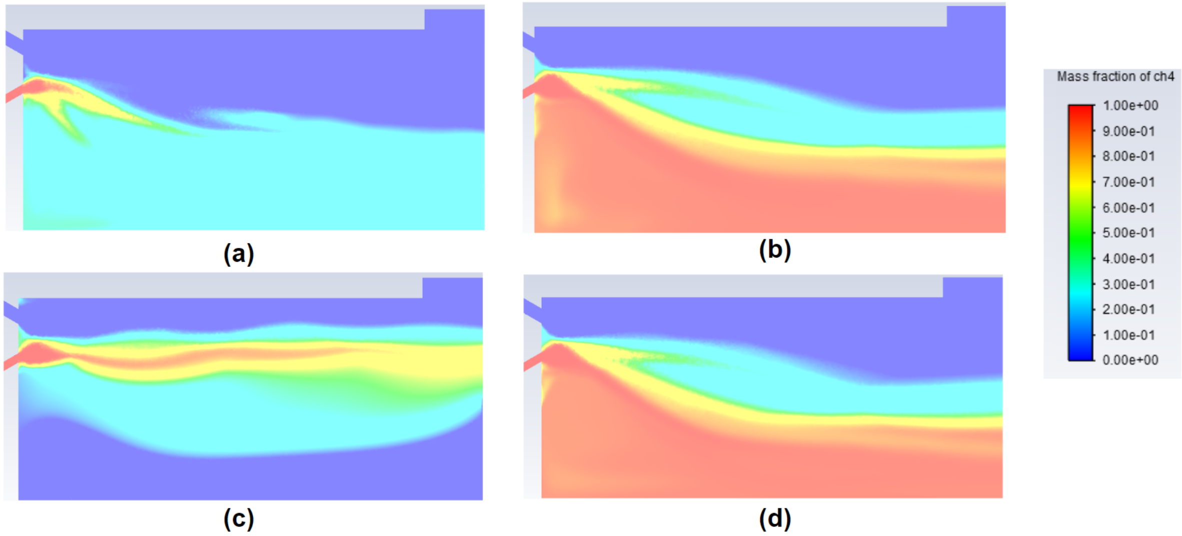

Figure 5.8: 25.4 mm coreless RDRE simulated velocity direction vectors colored by w_f at injector center plane for near stoichiometric test condition runs. a) $\phi = 0.41$, $\psi = 242$ kg/s/m^2. b) $\phi = 1.13$, $\psi = 172$ kg/s/m^2. c) $\phi = 1.81$, $\psi = 242$ kg/s/m^2. d) $\phi = 1.18$, $\psi = 504$ kg/s/m^2.

5.3.2 10 mm RDRE With Oxygen-Methane Propellant

The mass fraction of methane in the 10 mm RDRE was visualized in a similar way to the 25.4 mm RDRE. In figure 5.9, methane mass fraction at the center plane of the injector is compared across different ϕ and ψ conditions. The stoichiometric methane mass fraction is $w_f = 0.2$, which appears as light blue in the contour plots. A visible trend is that as ϕ was increased, the direction of the mixed layer at the injector changed from being pointed towards the center of the combustion chamber to instead moving towards the wall of the combustion chamber. This is likely due to changing momentum balance in the injectors as ϕ increases, with the fuel jet having more momentum relative to the oxidizer as ϕ increases. Compared with the 25.4 mm coreless RDRE, this effect was less pronounced, likely due to the shallower impingement angle of the oxidizer orifice, $11.3°$ as opposed to 30° for the 25.4 mm RDRE. Also as ϕ was increased, the mass fraction of methane at the center of combustion chamber visually increased. Comparing between different ψ at similar ϕ, high ψ as in figure 5.9b, and low ψ as in figure 5.9d, had similar momentum balance at the injector impingement point and similar downstream w_f distribution.

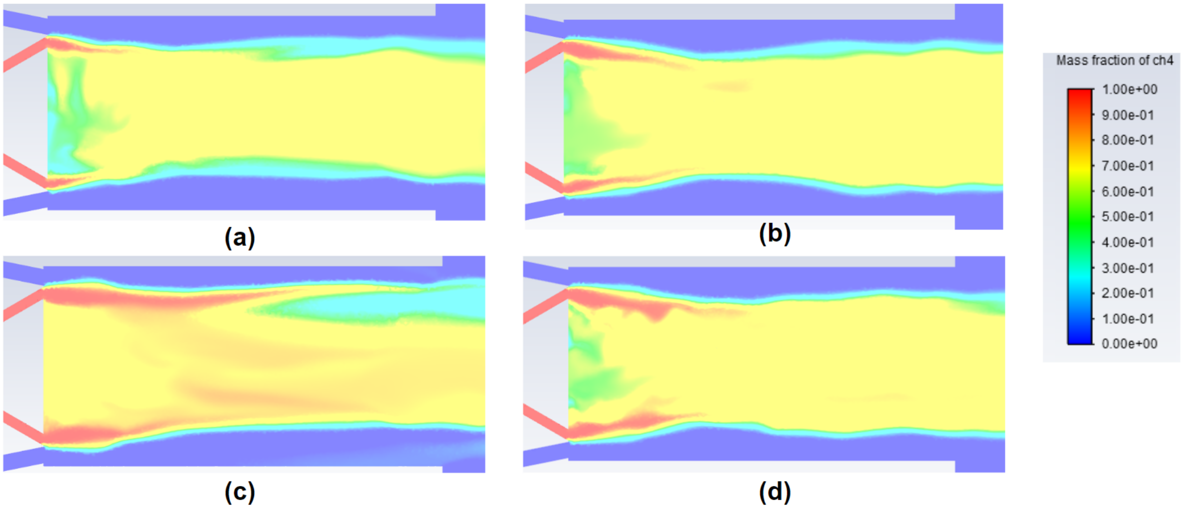

Figure 5.9: 10 mm RDRE simulated contours of methane w_f at injector center plane. a) $\phi = 0.83$, $\psi = 236\ \text{kg/s/m}^2$. b) $\phi = 1.12$, $\psi = 248\ \text{kg/s/m}^2$. c) $\phi = 1.75$, $\psi = 243\ \text{kg/s/m}^2$. d) $\phi = 1.14$, $\psi = 119\ \text{kg/s/m}^2$.

Figure 5.10 shows plots of velocity vectors colored by methane mass fraction for the 10 mm RDRE, similar to the 25.4 mm RDRE. Shown are the same simulation cases from figure 5.9. Across all four simulation cases, there was a region of recirculating oxygen-methane propellant at the center of the injector face which continued approximately one fourth the length of the combustion chamber. A region of reverse flow at the center of the combustion chamber exit is also seen in two of the simulation cases, figures 5.10a and 5.10b.

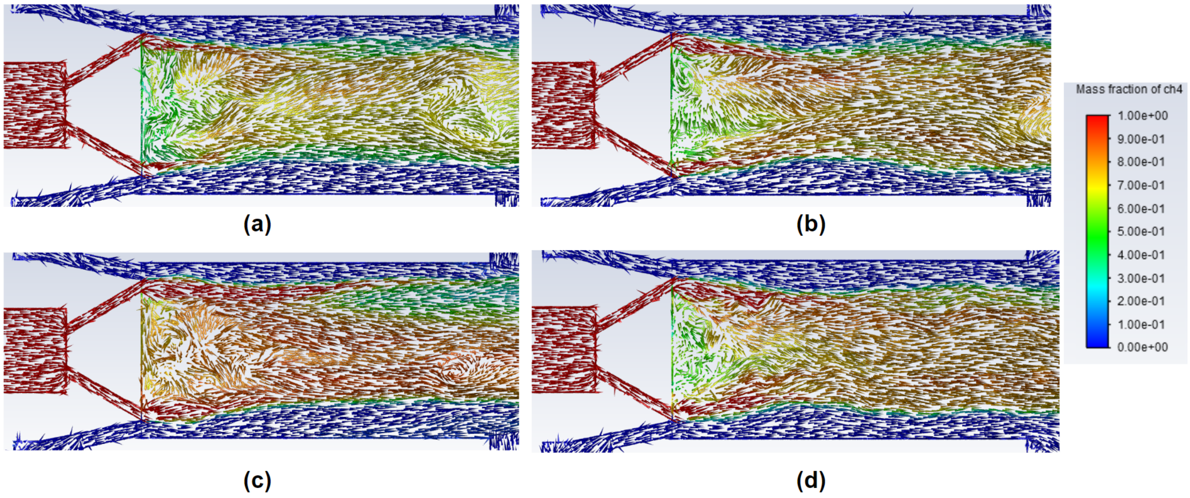

Figure 5.10: 10 mm RDRE simulated velocity direction vectors colored by methane w_f at injector center plane. a) $\phi = 0.83$, $\psi = 236 \text{ kg/s/m}^2$. b) $\phi = 1.12$, $\psi = 248 \text{ kg/s/m}^2$. c) $\phi = 1.75$, $\psi = 243 \text{ kg/s/m}^2$. d) $\phi = 1.14$, $\psi = 119 \text{ kg/s/m}^2$.

Methane mass fraction was also plotted across transverse planes at 0 mm, 1 mm, 4 mm, 16 mm, and 20 mm distances from the injector face. Mixing was seen to occur in a flower petal-like pattern very similar to in the 25.4 mm RDRE. This pattern was observed in transverse planes across all simulation cases for the 10 mm RDRE using oxygen-methane propellant.

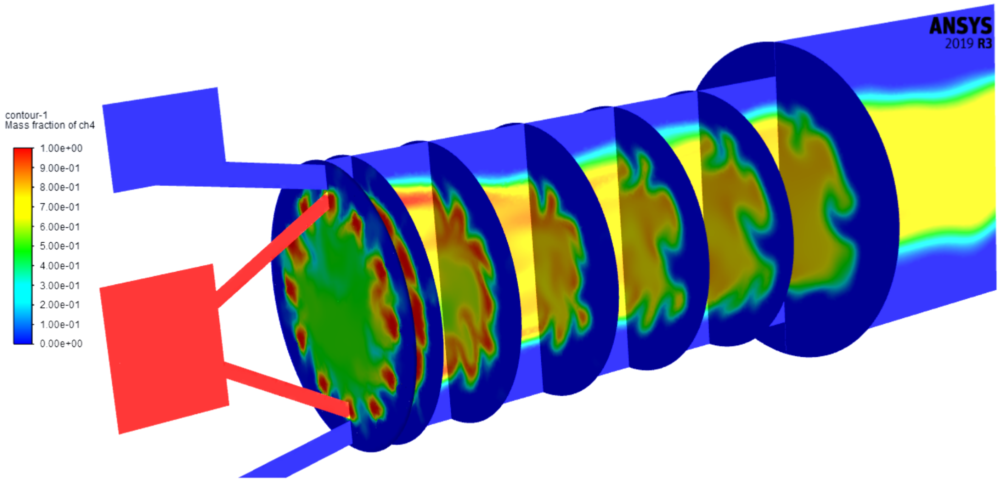

Figure 5.11: 10 mm RDRE simulated contours of methane w_f plotted over injector center plane and transverse planes at $x = 0$ mm, 1 mm, 4 mm, 16 mm, and 20 mm, $\phi = 1.12$, $\psi = 248 \text{ kg/s/m}^2$.

5.3.3 10 mm RDRE With Oxygen-Hydrogen Propellant

Similar to the previous sections, contours of w_f for the 10 mm RDRE using oxygen-hydrogen propellant were plotted on the injector center plane in figure 5.12. Contour plots for four different values of ϕ, three with the same ψ, and a fourth for near-stoichiometric conditions with a higher ψ. For hydrogen, the stoichiometric fuel mass fraction is $w_f = 0.11$, which corresponds to a darker light blue color than for methane. A clear difference is seen between all four w_f contours. As ϕ was increased, the momentum balance at the injector impingement point shifted from the mixed layer being pushed towards the center of the combustion chamber at low ϕ to being parallel with the combustion chamber walls at higher ϕ. Also, as ϕ was increased, the fraction of hydrogen at the center of the combustion increased with ϕ. The increase in ψ did not appear to make a significant difference in w_f distribution.

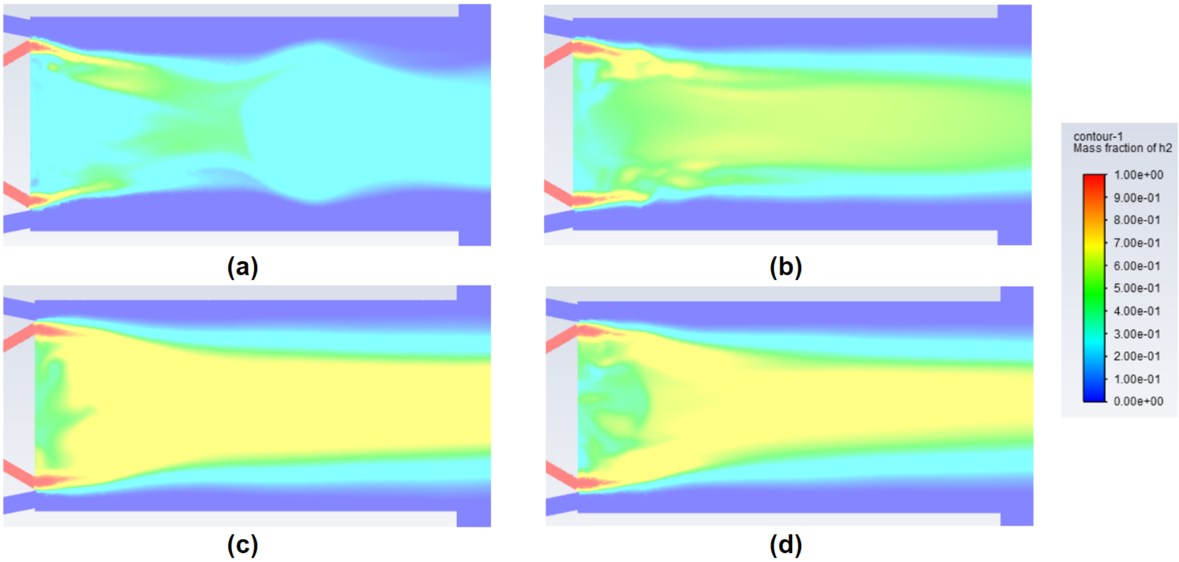

Figure 5.12: 10 mm RDRE simulated contours of hydrogen w_f at injector center plane. a) $\phi = 0.40$, $\psi = 186$ kg/s/m^2. b) $\phi = 0.77$, $\psi = 187$ kg/s/m^2. c) $\phi = 1.40$, $\psi = 180$ kg/s/m^2. d) $\phi = 1.01$, $\psi = 253$ kg/s/m^2.

For the same simulation cases as in figure 5.13, velocity direction vectors colored by hydrogen mass fraction are plotted on the injector center plane. All four simulations show an area of hydrogen rich recirculating flow near the center of the injector face, with this region spanning approximately one fourth of the length of the combustion chamber except for the $\phi = 0.77$, where it extended nearly to the combustion chamber exit. Another feature to note is that for the $\phi = 0.40$ simulation case, a second area of recirculating hydrogen rich flow occured at the center of the combustion chamber near its exit.

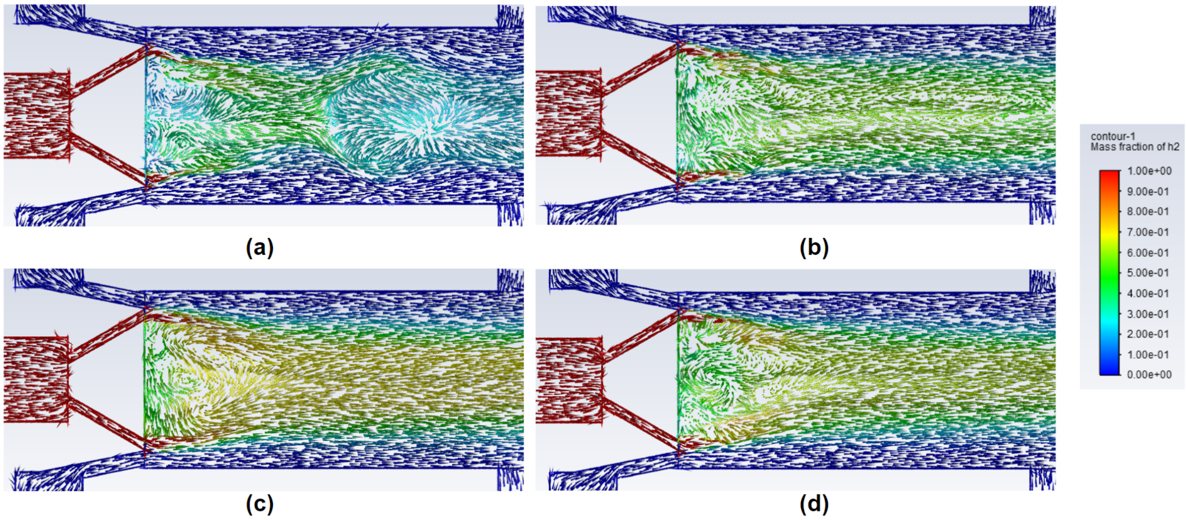

Figure 5.13: 10 mm RDRE simulated velocity direction vectors colored by hydrogen w_f at injector center plane. a) $\phi = 0.40$, $\psi = 186$ kg/s/m^2. b) $\phi = 0.77$, $\psi = 187$ kg/s/m^2. c) $\phi = 1.40$, $\psi = 180$ kg/s/m^2. d) $\phi = 1.01$, $\psi = 253$ kg/s/m^2.

Figure 5.14 shows w_f contours for the $\phi = 1.40$ and $\psi = 180$ kg/s/m^2 simulation case plotted on the injector center plane and transverse planes at the same distances from the injector face as in the previous section. Comparing with figure 5.11, the oxygen-hydrogen propellant simulations did not produce the flower petal-like mixing pattern as for the 10 mm RDRE and 25.4 mm RDRE with oxygen-methane propellant.

5.4 Mixedness

While plotting fuel mass fraction, w_f, is useful for comparing different configurations and simulation cases to stoichiometric conditions, stoichiometric conditions were not the goal of most engine tests. The mixedness parameter allowed comparison between simulation cases based on how closely the propellant mixuture approached the desired w_f for that engine test.

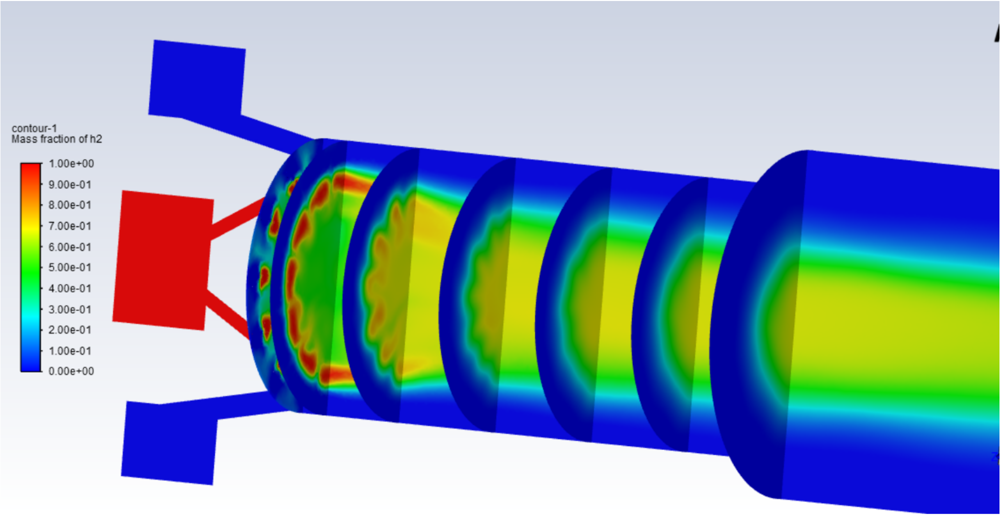

Figure 5.14: 10 mm RDRE simulated contours of hydrogen w_f plotted over injector center plane and transverse planes at $x = 0$ mm, 1 mm, 4 mm, 16 mm, and 20 mm, $\phi = 1.40$, $\psi = 180$ kg/s/m^2.

5.4.1 25.4 mm RDRE

The mixedness parameter was plotted in contour plots at the injector center plane similarly to how contours of w_f were reported. Because the contour plots in figure 5.5 were for near-stoichiometric simulations, the red layer corresponding to a mixedness of 1 in figure 5.15 compares well to the light blue mixed layer in figure 5.5.

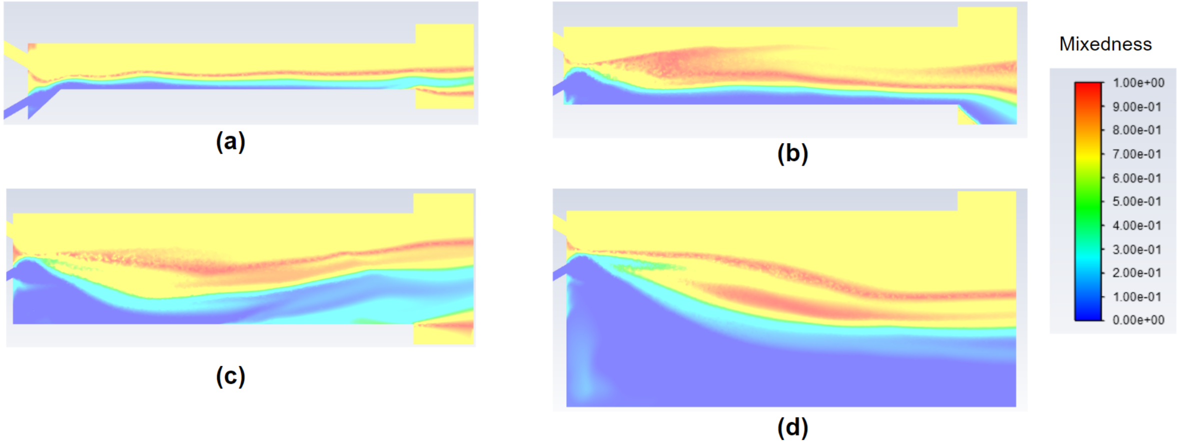

Figure 5.15: 25.4 mm RDRE simulated contours of ξ at injector center plane for near stoichiometric test condition runs. a) 3 mm annular, $\phi = 1.18$, $\psi = 288$ kg/s/m^2. b) 5 mm annular, $\phi = 1.18$, $\psi = 216$ kg/s/m^2. c) 7 mm annular, $\phi = 1.20$, $\psi = 238$ kg/s/m^2. d) Coreless, $\phi = 1.13$, $\psi = 172$ kg/s/m^2.

Another way that the distribution of mixedness across the combustion chamber was visualized by plotting the distribution of radius versus ψ weighted mixedness at multiple planes parallel to the injector face at $x = 0$, 5, 10, 15, 20, and 25 mm. Fig. 5.16 shows the radial distribution via a waterfall plot for two near stoichiometric cases of the test matrix for the coreless and 5 mm annular configurations, respectively. These plots compare well with the w_f contour plots shown in Fig. 5.5, with the peaks in the waterfall plots aligning with the location of the mixed layer indicated by the light blue region in the contour plots.

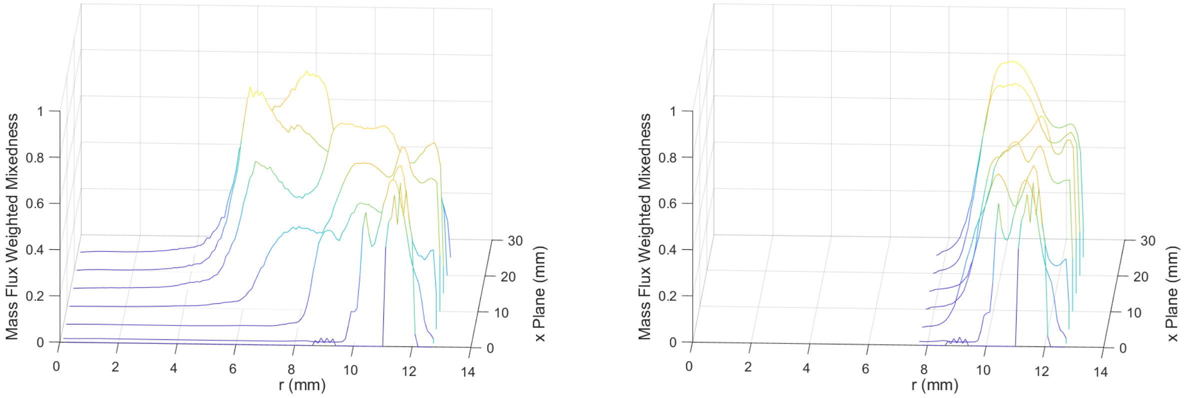

(a) (b)

Figure 5.16: 25.4 mm RDRE representative plots of ψ weighted mixedness at varying radius and x planes. a) Coreless $\phi = 1.13$, $\psi = 172$ kg/s/m^2. b) 5 mm annular $\phi = 1.18$, $\psi = 216$ kg/s/m^2.

The mixedness of the propellant mixture as a whole as it moves downstream of the injector was quantified by taking a ψ weighted average of mixedness across all the cells at each of the previously described planes. The resulting average weighted mixedness data versus x are plotted in Figs. 5.17 and 5.18. Figure 5.17 shows these data for conditions near stoichiometric for all the engine configurations. For these simulations, the 7 mm annular configuration mixes by far the most quickly, followed by the 3 mm configuration, with the 5 mm and coreless configuration mixing least quickly.

Figure 5.18a shows simulations at low ϕ values, where the 7 mm annular configuration still mixes the fastest, but the 5 mm configuration mixes the second most quickly, and the 3 mm the slowest. Figure 5.18b shows simulations at high ϕ values, where the 3 mm configuration can be seen to mix the fastest, with comparable 7 mm data being unavailable.

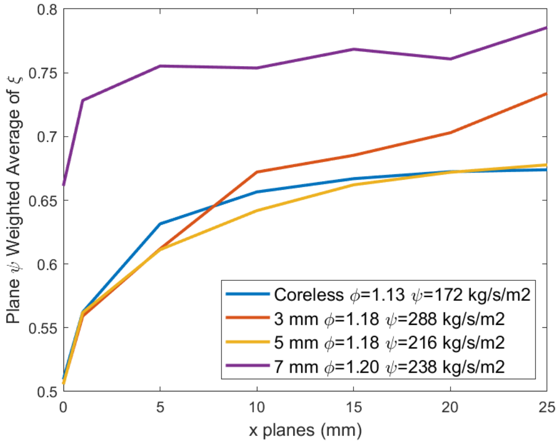

Figure 5.17: 25.4 mm RDRE plot of simulated ψ weighted averages of mixedness over planes with varying x for simulations near stoichiometric.

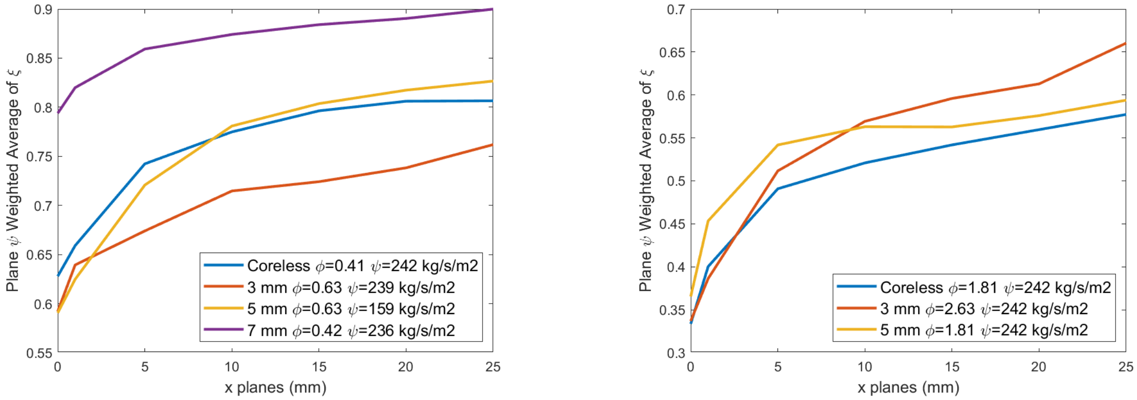

(a)

(b)

Figure 5.18: 25.4 mm RDRE simulated ψ weighted averages of mixedness over planes with varying x. a) Low ϕ. b) High ϕ.

5.4.2 10 mm RDRE With Oxygen-Methane Propellant

Similar to the 25.4 mm RDRE, the mixedness results for the 10 mm RDRE were reported as contour plots as shown in figure 5.19. Notably, the red fully mixed layer location did not qualitatively appear to vary significantly across varying ϕ and ψ.

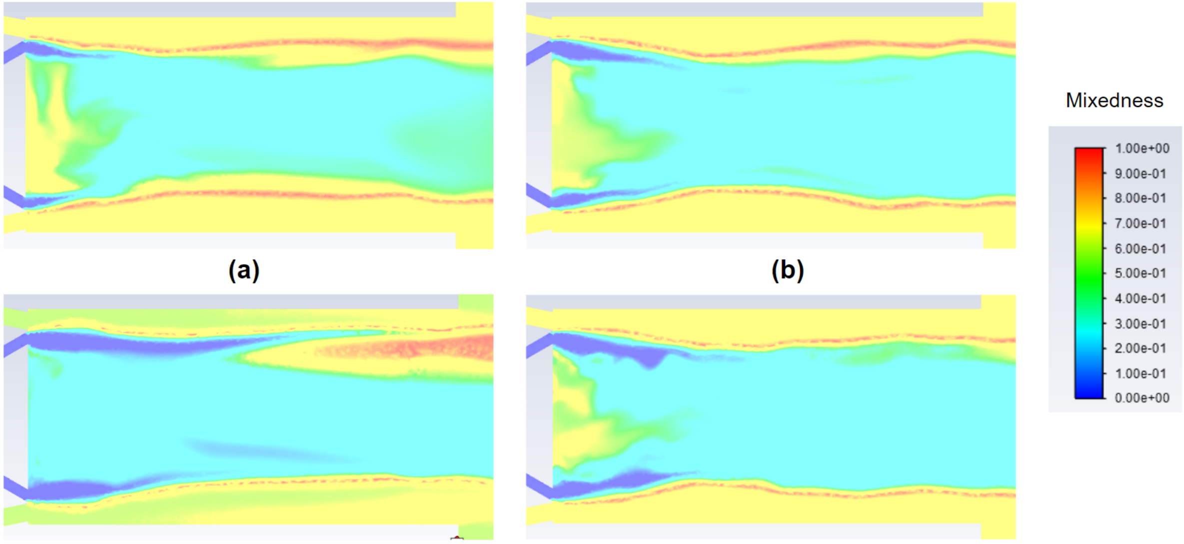

Figure 5.19: 10 mm RDRE simulated contours of methane ξ at injector center plane. a) $\phi = 0.83$, $\psi = 236\ \text{kg/s/m}^2$. b) $\phi = 1.12$, $\psi = 248\ \text{kg/s/m}^2$. c) $\phi = 1.75$, $\psi = 243\ \text{kg/s/m}^2$. d) $\phi = 1.14$, $\psi = 119\ \text{kg/s/m}^2$.

As with the 25.4 mm RDRE, the mass flux weighted average of mixedness was averaged radially across transverse planes 0, 1, 4, 8, 12, 16, and 20 mm away from the injector. This method offers a more quantifiable method of determining the location of the mixed layer of propellant. In figure 5.20, this weighted mixedness distribution is compared between a simulation at low ϕ and at high ϕ. The weighted averaged mixed layer can be seen to trend more towards the center of the combustion chamber for a lower ϕ in these plots.

Mass flux weighted mixedness averaged over the entirety of each transverse plane is compared between each simulation case in figure 5.24. This compares how fully the propellant mixture for each simulation approaches the desired w_f for that simulation. ϕ appears to have the largest effect on how well propellants are mixed with lower ϕ resulting in better mixing, and ψ having little effect.

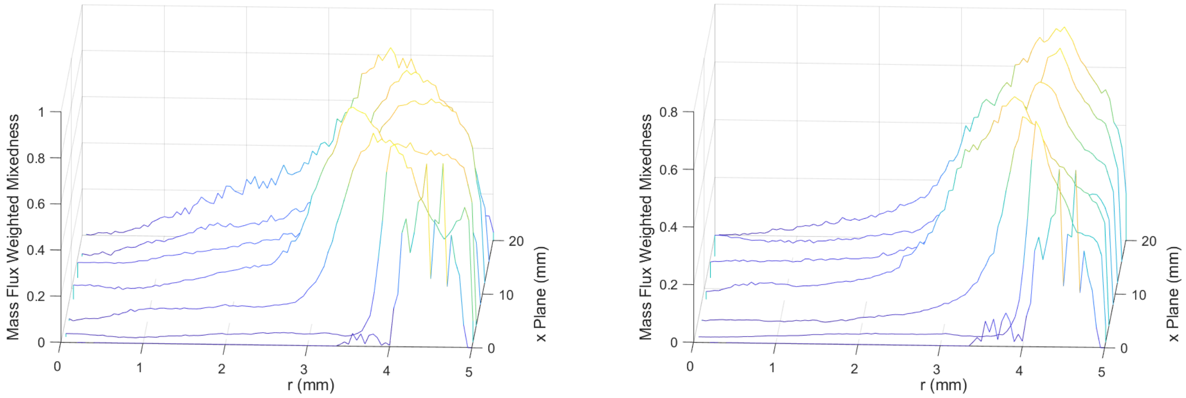

(a) (b)

Figure 5.20: Representative plots of ψ weighted mixedness at varying radius and x planes for 10 mm RDRE with oxygen-methane propellant. a) $\phi = 0.83$, $\psi = 236$ kg/s/m^2. b) $\phi = 1.75$, $\psi = 243$ kg/s/m^2.

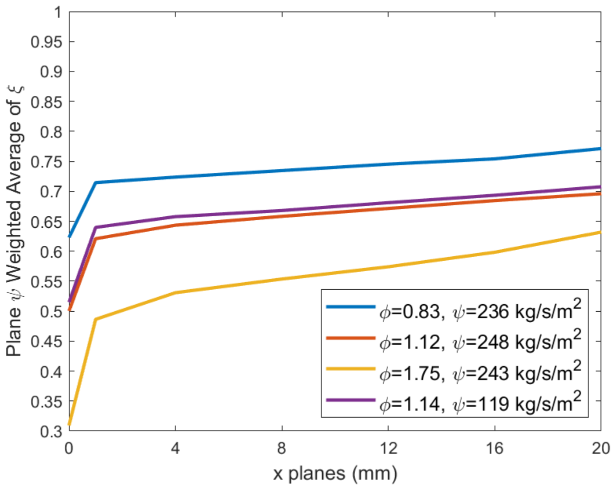

Figure 5.21: Plot of simulated ψ weighted averages of mixedness over planes with varying x for oxygen-methane propellant 10 mm RDRE simulations varying ϕ and ψ.

5.4.3 10 mm RDRE With Oxygen-Hydrogen Propellant

As with the 10 mm RDRE with oxygen-methane propellant, mixednes was plotted in contour plots for four representative simulations for the 10 mm RDRE with oxygen-hydrogen propellant. The location of the mixed layer visually is relatively consistent across each simulation, while the mixedness of the region at the center of the combustion chamber decreases with ϕ.

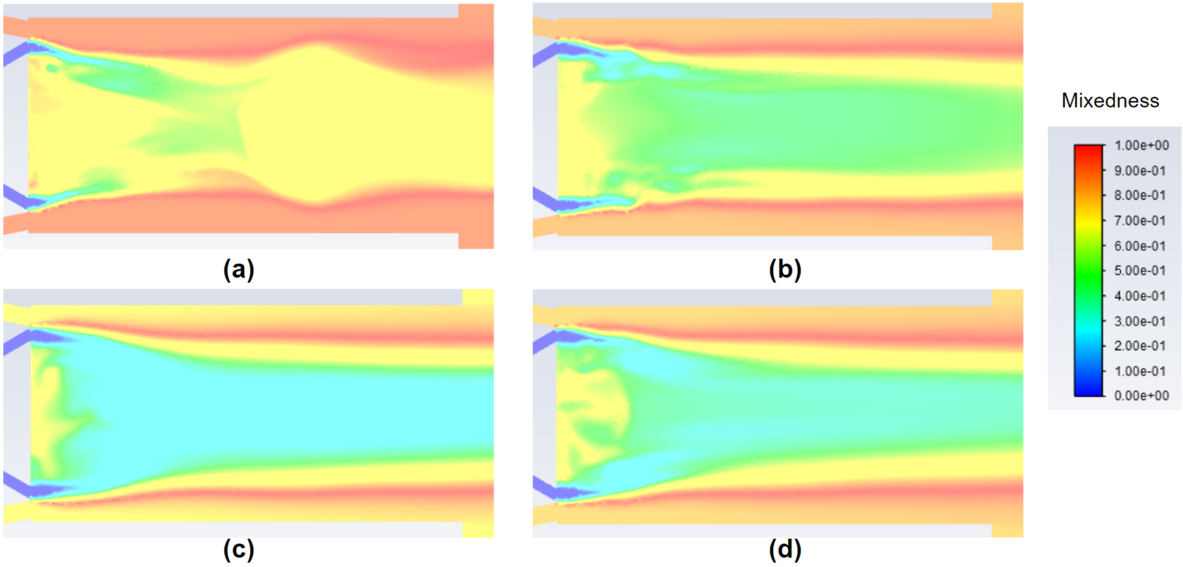

Figure 5.22: 10 mm RDRE simulated contours of hydrogen ξ at injector center plane. a) $\phi = 0.40$, $\psi = 186\ \text{kg/s/m}^2$. b) $\phi = 0.77$, $\psi = 187\ \text{kg/s/m}^2$. c) $\phi = 1.40$, $\psi = 180\ \text{kg/s/m}^2$. d) $\phi = 1.01$, $\psi = 253\ \text{kg/s/m}^2$.

Examining the plots of ψ weighted mixedness radial distributions over varying transverse planes in figure 5.23, not much difference in the position of the mixed layer is seen between high ϕ and low ϕ. ϕ did however effect the plane-averaged mixing characteristics, with lower values of ϕ experiencing more complete mixing. Comparing with the 10 mm RDRE using oxygen-methane propellant, plane-averaged mixedness was much higher across all simulations for oxygen-hydrogen propellant in the same engine.

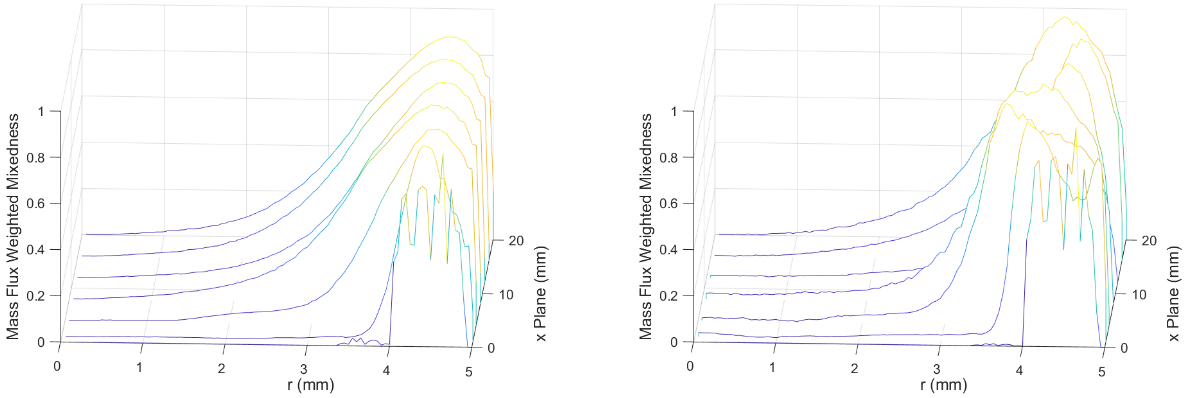

(a)

(b)

Figure 5.23: Representative plots of ψ weighted mixedness at varying radius and x planes for 10 mm RDRE with oxygen-hydrogen propellant. a) $\phi = 0.39$, $\psi = 186$ kg/s/m^2. b) $\phi = 1.39$, $\psi = 181$ kg/s/m^2.

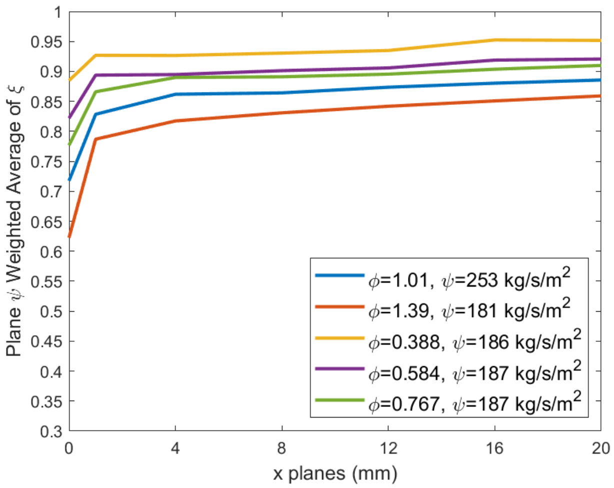

Figure 5.24: Plot of simulated ψ weighted averages of mixedness over planes with varying x for oxygen-hydrogen propellant 10 mm RDRE simulations varying ϕ and ψ.

5.5 High-Speed Video

High-speed video was taken of hot fire tests with the camera pointing directly into the combustion chamber. For the 25.4 mm RDRE, video was recorded at 240,000 frames per second. For the 10 mm RDRE, video was recorded at 360,000 frames per second for oxygen-methane propellant tests, and 1,000 frames per second for oxygen-hydrogen propellant tests. Representative still frames from high-speed video is shown in figures 5.25, 5.26, and 5.27, covering a range of ϕ values from low to high. Hot gas produced by the detonation wave is visible as regions of high luminosity. Notably, in some video frames, the oxidizer injector orifices were also visible in some areas. While the results of numerical simulations performed in this study were for pre-ignition conditions and do not represent the flow field in the RDRE during operation, high speed video was analyzed to compare pre-ignition mixing trends with hot fire detonation wave radial position. Coreless configurations were chosen for this comparison as they were seen to be the most affected by changes in injector momentum balance.


(a) (b) (c)

Figure 5.25: Still frames from high-speed video of 25.4 mm RDRE coreless configuration hot fire tests. a) $\phi = 41$, $\psi = 240$ kg/s/m^2. b) $\phi = 1.17$, $\psi = 242$ kg/s/m^2. c) $\phi = 1.81$, $\psi = 242$ kg/s/m^2.


(a) (b) (c)

Figure 5.26: Still frames from high-speed video of methane-fueled 10 mm RDRE hot fire tests. a) $\phi = 98$, $\psi = 249$ kg/s/m^2. b) $\phi = 1.15$, $\psi = 249$ kg/s/m^2. c) $\phi = 1.54$, $\psi = 247$ kg/s/m^2.

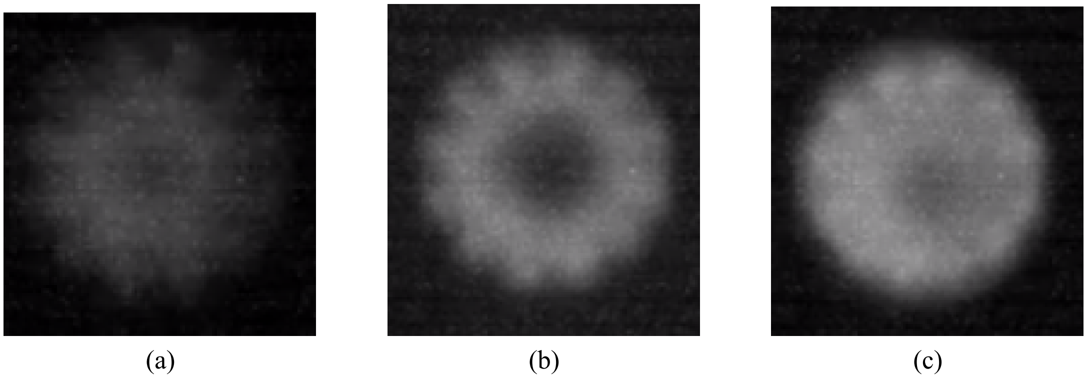

Figure 5.27: Still frames from high-speed video of hydrogen-fueled 10 mm RDRE hot fire tests. a) $\phi = 0.39$, $\psi = 186$ kg/s/m^2. b) $\phi = 0.77$, $\psi = 187$ kg/s/m^2. c) $\phi = 1.3$, $\psi = 187$ kg/s/m^2.

Each of the representative high-speed videos chosen were analyzed using MATLAB video analysis tools. Frames from each video were cropped to the luminous circle that outlined the walls of the combustion chamber, and each pixel grouped by radius from the center of the combustion chamber. Pixel luminosities were then averaged by radius to produce a curve of radius versus average luminosity. This average curve was then used to determine the radius of peak luminosity.

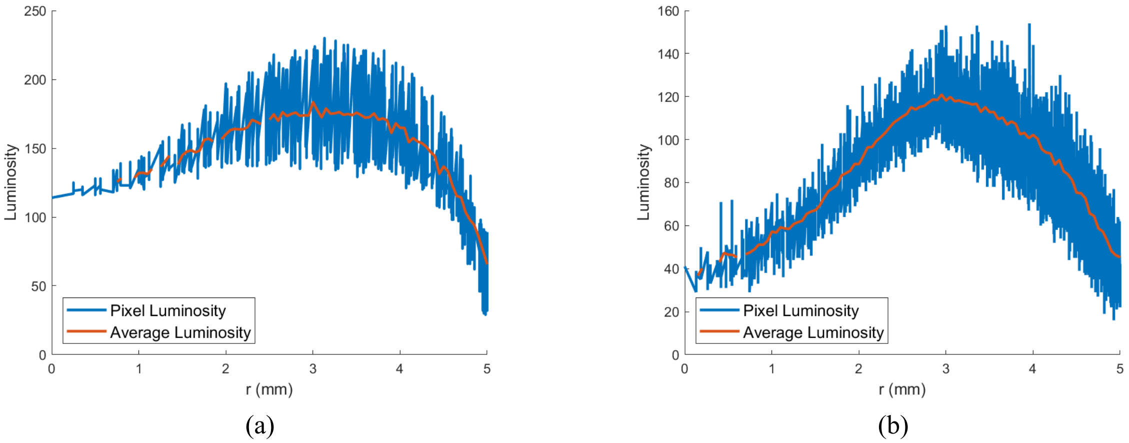

Figure 5.28: Representative radius vs. luminosity plots used to find radius of peak luminosity. a) 10 mm RDRE, oxygen-methane propellant, $\phi = 1.15$, $\psi = 249$ kg/s/m^2. b) 10 mm RDRE, oxygen-hydrogen propellant, $\phi = 0.77$, $\psi = 187$ kg/s/m^2.

Radii of peak luminosity are compiled in table 5.3. A trend seen in all three engine configurations examined is that the radius of peak luminosity increased with increasing ϕ. This trend was especially strong in the 10 mm RDRE with oxygen-hydrogen propellant and was clearly visible in high-speed video. The trend was not quite as strong in the 10 mm RDRE with oxygen-methane propellant, being not clearly visible in the high-speed video, but still significant in the video processing data. The 25.4 mm coreless RDRE displayed the trend of increasing peak luminosity radius between $\phi = 0.41$ and $\phi = 1.17$, but not between $\phi = 1.17$ and $\phi = 1.81$. This trend correlates with the plots of fuel mass fraction reported in section 5.3, where increasing ϕ led to a larger fraction of fuel at the combustion chamber center and a injector impingement point momentum balance biased more towards the combustion chamber outer wall.

Table 5.3: Peak luminosity results from high-speed video

Engine Config.	Run Number	ϕ	Peak Luminosity Radius (mm)
25.4 mm coreless	131	0.41	9.1
	84	1.17	11.3
	89	1.81	10.6
10 mm O_2/CH_4	244	0.98	2.9
	134	1.15	3.4
	252	1.54	3.7
10 mm O_2/H_2	31	0.39	1.8
	33	0.77	2.9
	29	1.30	3.1

Chapter 6

Conclusion

Simulations of propellant injection into four different annular combustor configurations of a 25.4-mm RDRE were carried out to study the influence of gap width on the mixing process. The mixedness parameter used herein proved to be an effective figure of merit to compare the uniformity of the flows. For a given mass flux and equivalence ratio, the smallest gap (3-mm) was found to mix the quickest in the 25.4-mm-long combustors. In all but one case, however, the planar average of the mass flux weighted mixedness was around 70% to 80% at the exit of the combustor.

Similarly, simulations were carried out of propellant injection into a 10 mm RDRE to study the influence of different propellant combinations on the mixing process and compare with the 25.4 mm RDRE. As with the 25.4 mm RDRE, the mixedness parameter proved to be an effective means of comparison. Equivalence ratio ϕ was found to have the largest influence on mixing across both propellant combinations. Oxygen-hydrogen propellant was found to mix more completely than oxygen-methane propellant. Compared with the 25.4 mm RDRE, the 10 mm RDRE with oxygen-methane propellant had similar bulk mixing characteristics, and the 10 mm RDRE with oxygen-methane propellant had the most complete mixing.

Simulations of all engine configurations and propellant configurations were verified through comparison of pressure data from simulations with pressure data from experiment. Wall static pressure measurements compared well across all simulations performed where comparable experimental data was available. Plenum pressure data, converted into discharge coefficients, compared relatively well with experimental values, and was consistent between simulations.

Contour plots created through simulations showed that coreless configurations had propellant mixing distributions most influenced by injector momentum balance. Radial luminosity distribution of high speed video of experimental hot fire testing was compared with injector momentum balance trends seen in simulations. The radius of peak luminosity from high speed video was found to increase with fuel equivalence ratio in the same way that the radius of the stoichiometrically mixed propellant layer increased with increasing fuel equivalence ratio in pre-ignition simulations.

The techniques outlined here are an effective way of quantifying and visualizing pre-ignition propellant mixing in the 25.4 mm and 10 mm RDREs in a manner that may be useful in determining under what conditions propellant ignition difficulties may be expected to arise. These techniques also have provided insight into the effectiveness of current injector designs and may be used to evaluate future injector designs.

Bibliography

[1] Koch, J. V., "Nonlinear Dynamics of Rotating Detonation Waves," Ph.D. thesis, William E. Boeing Department of Aeronautics and Astronautics, University of Washington, Seattle, WA, 2020. URL `http://hdl.handle.net/1773/45431`.

[2] Sutton, G. P., and Biblarz, O., *Rocket Propulsion Elements*, 9th ed., John Wiley & Sons, Inc., Hoboken, NJ, 2017, Chap. 8.1.

[3] Knowlen, T., C amd Mundt, and Kurosaka, M., "Experimental Results for 25-mm and 51-mm Rotating Detonation Rocket Engine Combustors," *Shock Waves*, April 2023. doi:https://doi.org/10.1007/s00193-023-01120-x.

[4] Mundt, T. J., Chang, L., Ikeda, M., Menn, D., Knowlen, C., and Kurosaka, M., "Annular Gap Width Variation in 25-mm Rotating Detonation Rocket Engine," *AIAA Paper 2023-1103*, January 2023. doi:10.2514/6.2023-1103.

[5] Bykovskii, F. A., Zhdan, S. A., and Vedermikov, E. F., "Continuous Spin Detonations," *Journal of Propulsion and Power*, Vol. 22, No. 6, 2006, pp. 1204, 1216. doi:10.2514/1.17656.

[6] Lu, F. K., and Braun, E. M., "Rotating Detonation Wave Propulsion: Experimental Challenges, Modeling, and Engine Concepts," *Journal of Propulsion and Power*, Vol. 30, No. 5, 2014, pp. 1125, 1142. doi:10.2514/1.B34802.

[7] Lee, J. H. S., *The Detonation Phenomenon*, Cambridge University Press, NY, 2008. doi:10.1017/CBO9780511754708.

[8] Rankin, B. A., Fotia, M. L., Naples, A. G., Stevens, C. A., Hoke, J. L., Kaemming, T. A., Theuerkauf, S. W., and Schauer, F. R., “Overview of Performance, Application, and Analysis of Rotating Detonation Engine Technologies,” *Journal of Propulsion and Power*, Vol. 33, No. 1, 2017, pp. 131, 143. doi:10.2514/1.B36303.

[9] Smith, R. D., and Stanley, S. B., “Experimental Investigation of Rotating Detonation Rocket Engines for Space Propulsion,” *Journal of Propulsion and Power*, Vol. 37, No. 3, 2021, pp. 463, 473. doi:10.2514/1.B37959.

[10] Burden, A. M., Burke, R. F., Rezzag, T., Jacobson, J. O., Schuetz, S., and Ahmed, K. A., “Characterization of Injection Mixing in The Rotating Detonation Rocket Engine,” *AIAA Paper 2023-0572*, January 2023. doi:10.2514/6.2023-0572.

[11] Prakash, S., Raman, V., Lietz, C. F., Hargus, W. A., and Schumaker, S. A., “Numerical simulation of a methane-oxygen rotating detonation rocket engine,” *Proceedings of the Combustion Institute*, Vol. 38, No. 3, 2021, pp. 3777–3786. doi:https://doi.org/10.1016/j.proci.2020.06.288.

[12] Bohon, M. D., Bluemner, R., Paschereit, C. O., and Gutmark, E. J., “Experimental Study of Reactants Mixing in Model Rotating Detonation Engine Geometries,” *AIAA Paper 2017-4739*, July 2017. doi:10.2514/6.2017-4739.

[13] Washington, M. R., Koch, J. V., Kurosaka, M., and Knowlen, C., “Radial Injector Mixing Effects on Detonation Zone Position in Rotating Detonation Engine,” *AIAA Paper 2019-4131*, August 2019. doi:10.2514/6.2019-4131.

[14] Knowlen, C., Mundt, T. J., and Kurosaka, M., “Experimental Results for Geometrically Scaled Rotating Detonation Rocket Engines,” *AIAA SCITECH Forum*, January 2023. doi:10.2514/6.2023-0354.

[15] Heath, J. D., “Generating Detonation Waves in an Annulus via Phased Adiabatic Shocks,”

Master's thesis, William E. Boeing Department of Aeronautics and Astronautics, University of Washington, Seattle, WA, 2015. URL `http://hdl.handle.net/1773/33548`.

[16] Washington, M. R., "Radial Injector Mixing Effects on Detonation Zone Position in Rotating Detonation Engine," Master's thesis, William E. Boeing Department of Aeronautics and Astronautics, University of Washington, Seattle, WA, 2019. URL `http://hdl.handle.net/1773/43625`.

[17] Boening, J. A., Wheeler, E. A., Heath, J. D., Koch, J. V., Mattick, A. T., Breidenthal, R. E., Knowlen, C., and Kurosaka, M., "Rotating Detonation Engine Using a Wave Generator and Controlled Mixing," *Journal of Propulsion and Power*, Vol. 34, No. 6, 2018, pp. 1364–1375. doi:10.2514/1.B36603.

[18] ANSYS, Inc., *ANSYS® Fluent Revision 19.5.0*, Southpointe 2600 ANSYS Drive, Canonsburg, PA, 2019.

[19] ANSYS, Inc., *ANSYS® Fluent Theory Guide Release 2023 R1*, Southpointe 2600 ANSYS Drive, Canonsburg, PA, 2023.

[20] Rodriguez, S., *Applied Computational Fluid Dynamics and Turbulence Modeling*, 1st ed., Springer, Cham, Switzerland, 2019, Chaps. 4, 6.

[21] Cengel, Y. A., and Boles, M. A., *Thermodynamics, an Engineering Approach*, 6th ed., McGraw-Hill, New York, NY, 2008, Chaps. 17, Appendix 1.

Appendix A

Additional Fuel Mass Fraction Contours

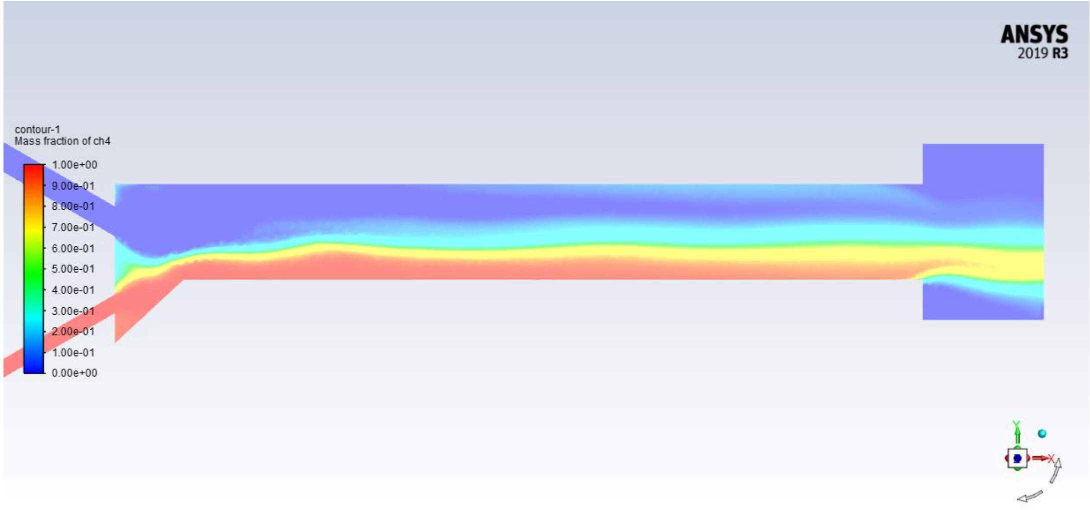

Figure A.1: Injector center plane contours of w_f for 25.4 mm RDRE 3-mm-gap configuration, run 291.

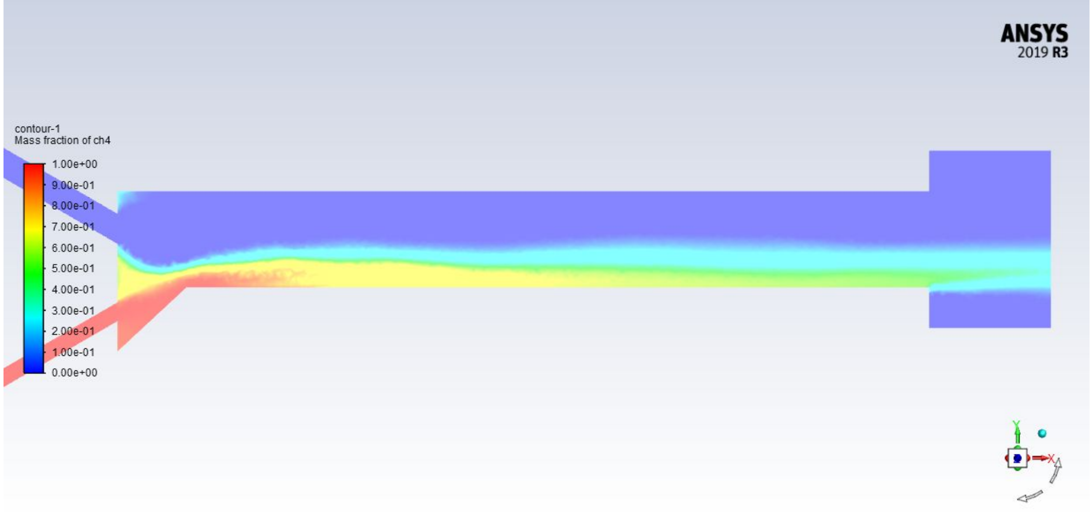

Figure A.2: Injector center plane contours of w_f for 25.4 mm RDRE 3-mm-gap configuration, run 304.

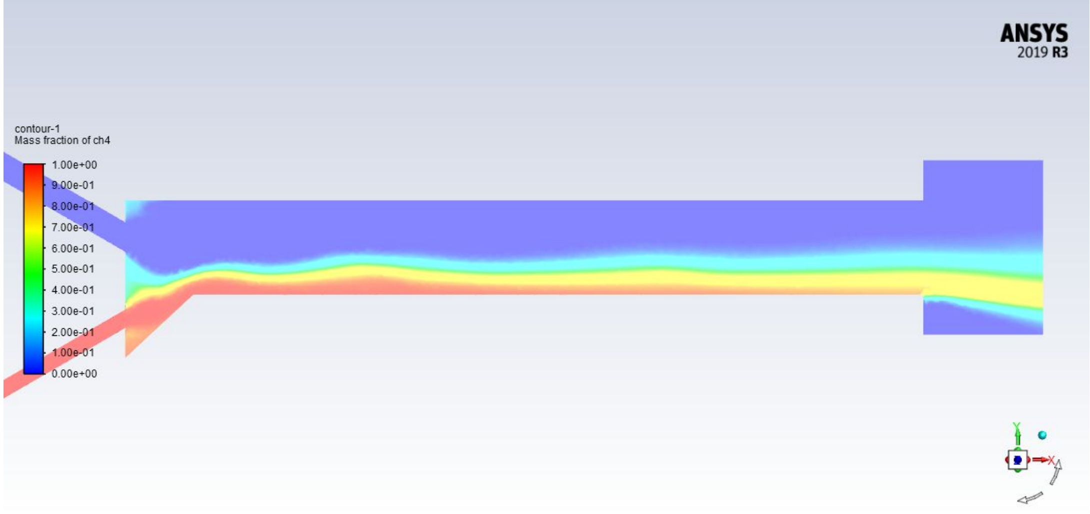

Figure A.3: Injector center plane contours of w_f for 25.4 mm RDRE 3-mm-gap configuration, run 319.

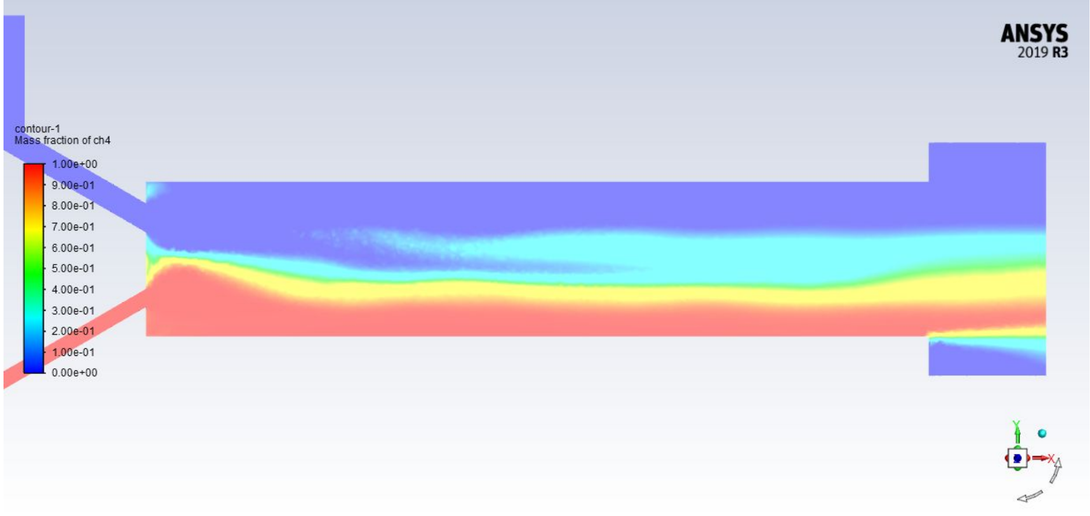

Figure A.4: Injector center plane contours of w_f for 25.4 mm RDRE 5-mm-gap configuration, run 192.

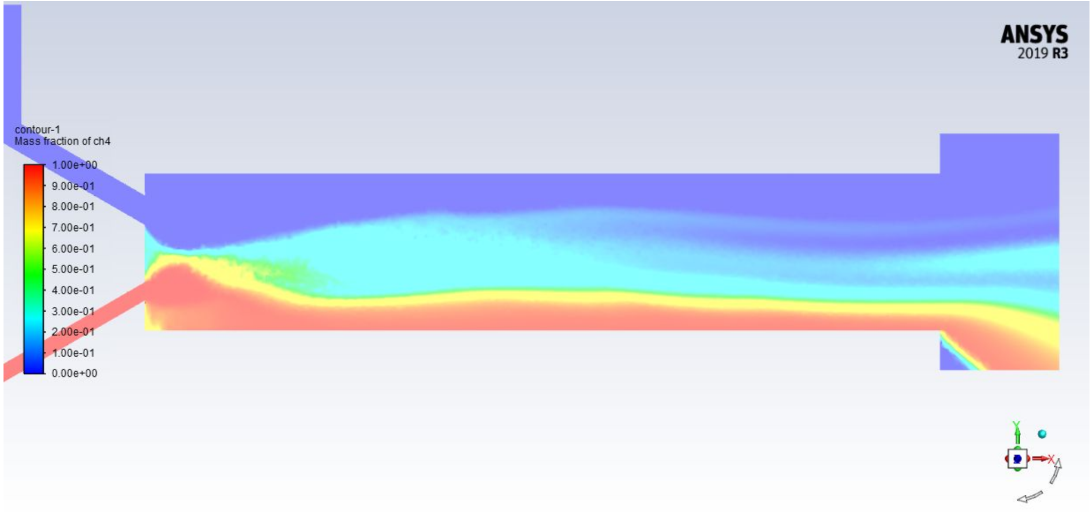

Figure A.5: Injector center plane contours of w_f for 25.4 mm RDRE 5-mm-gap configuration, run 234.

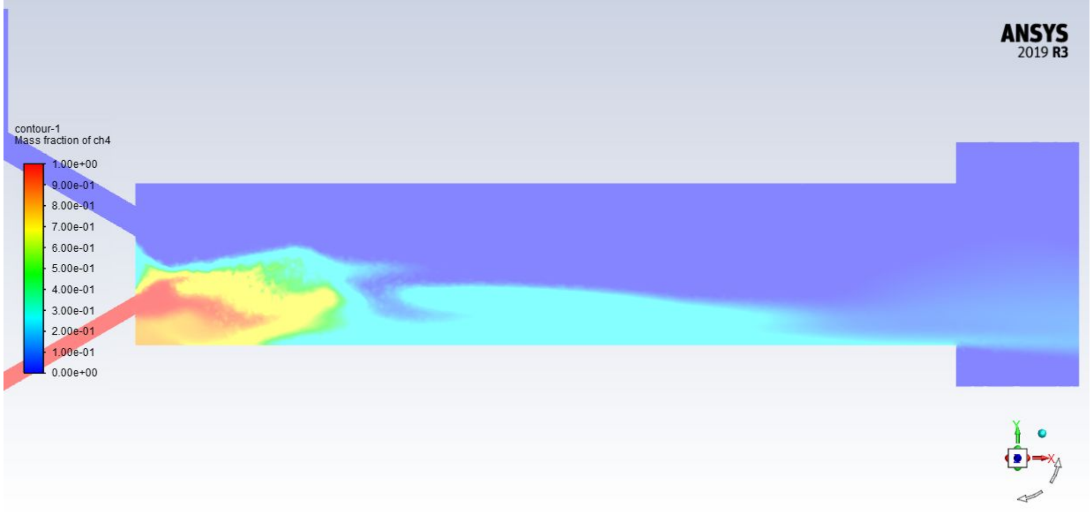

Figure A.6: Injector center plane contours of w_f for 25.4 mm RDRE 5-mm-gap configuration, run 408.

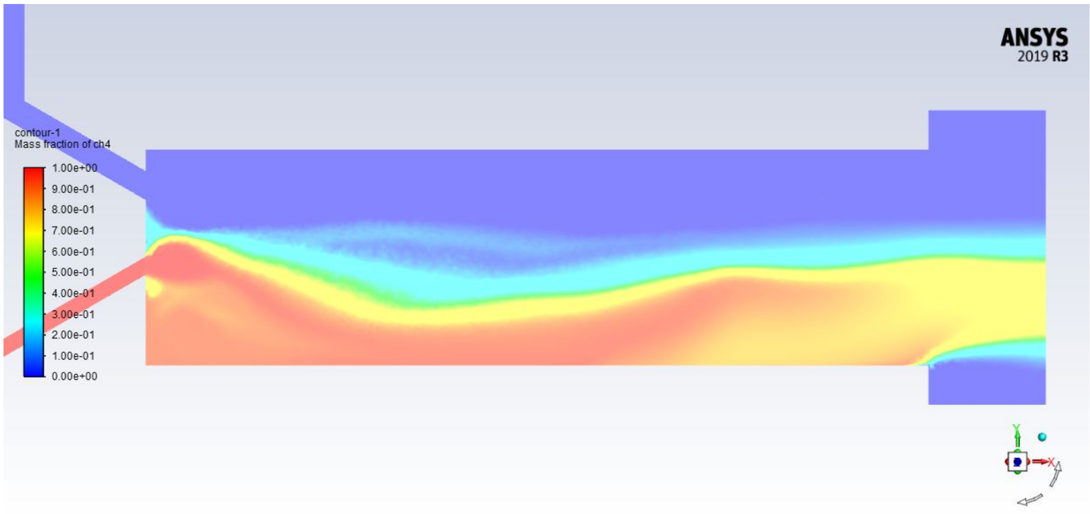

Figure A.7: Injector center plane contours of w_f for 25.4 mm RDRE 7-mm-gap configuration, run 337.

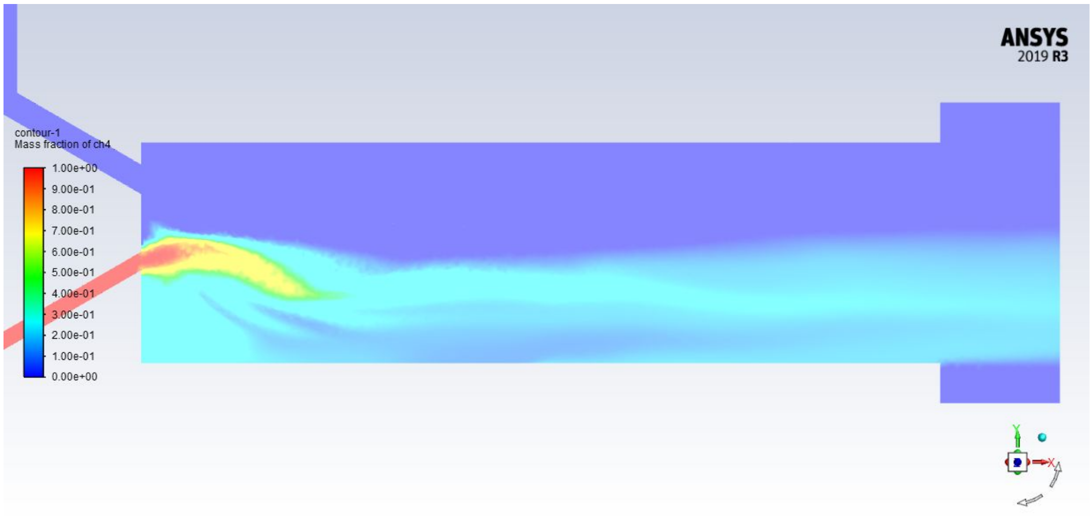

Figure A.8: Injector center plane contours of w_f for 25.4 mm RDRE 7-mm-gap configuration, run 338.

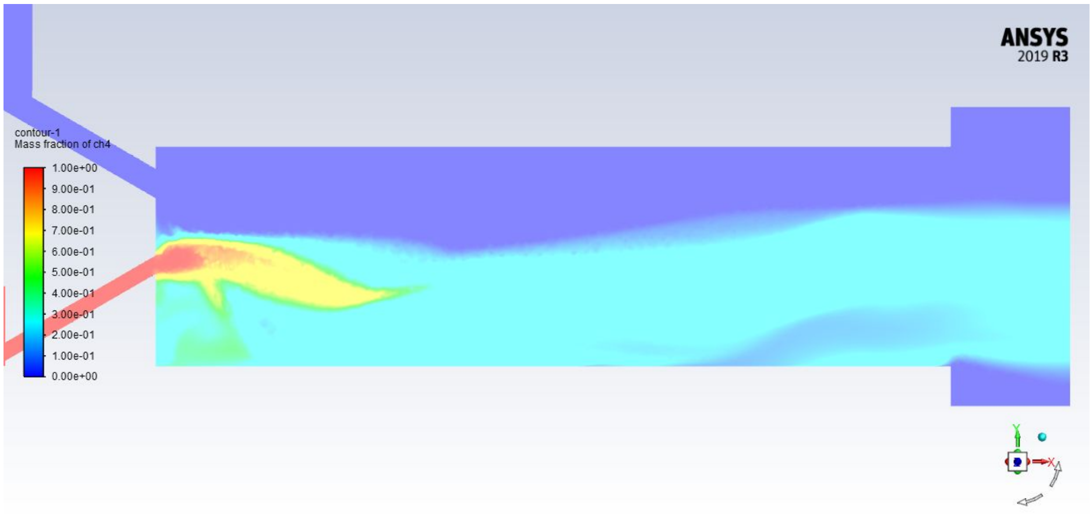

Figure A.9: Injector center plane contours of w_f for 25.4 mm RDRE 7-mm-gap configuration, run 342.

Appendix B

Additional Mixedness Contours

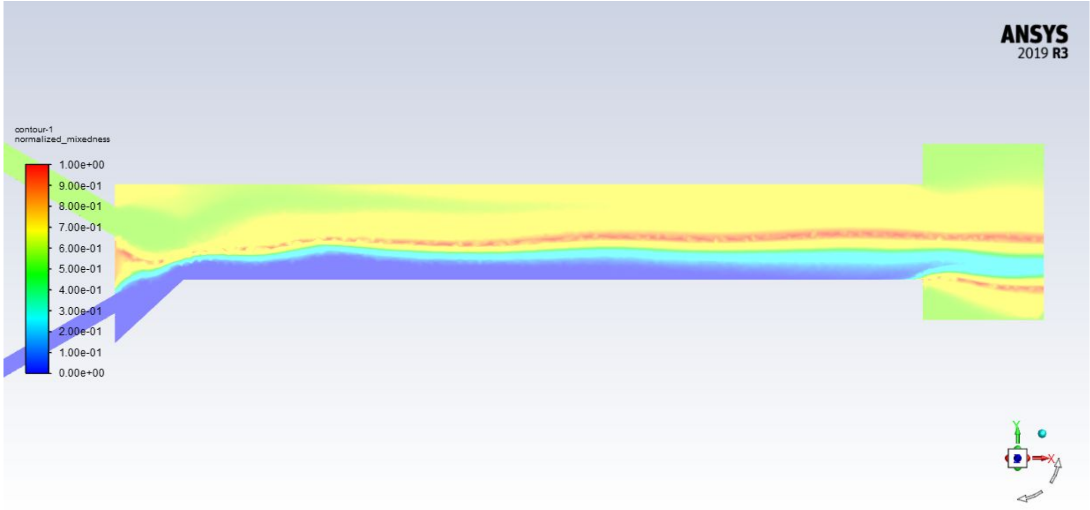

Figure B.1: Injector center plane contours of ξ for 25.4 mm RDRE 3-mm-gap configuration, run 291.

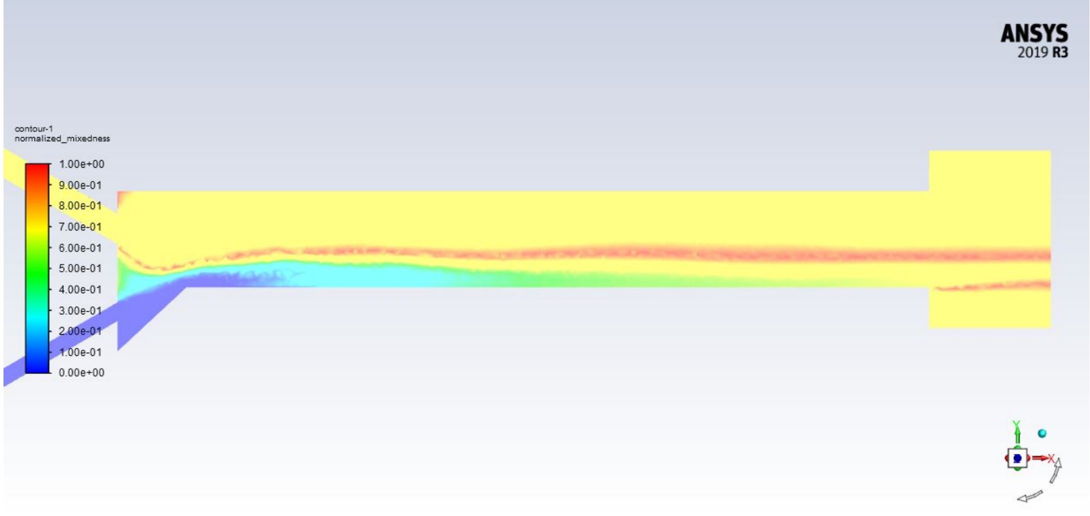

Figure B.2: Injector center plane contours of ξ for 25.4 mm RDRE 3-mm-gap configuration, run 304.

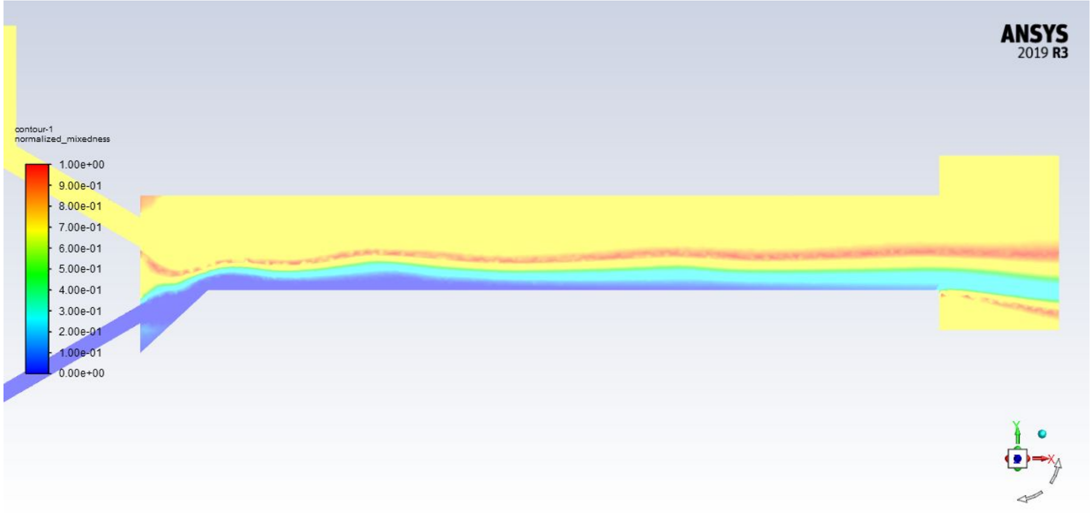

Figure B.3: Injector center plane contours of ξ for 25.4 mm RDRE 3-mm-gap configuration, run 319.

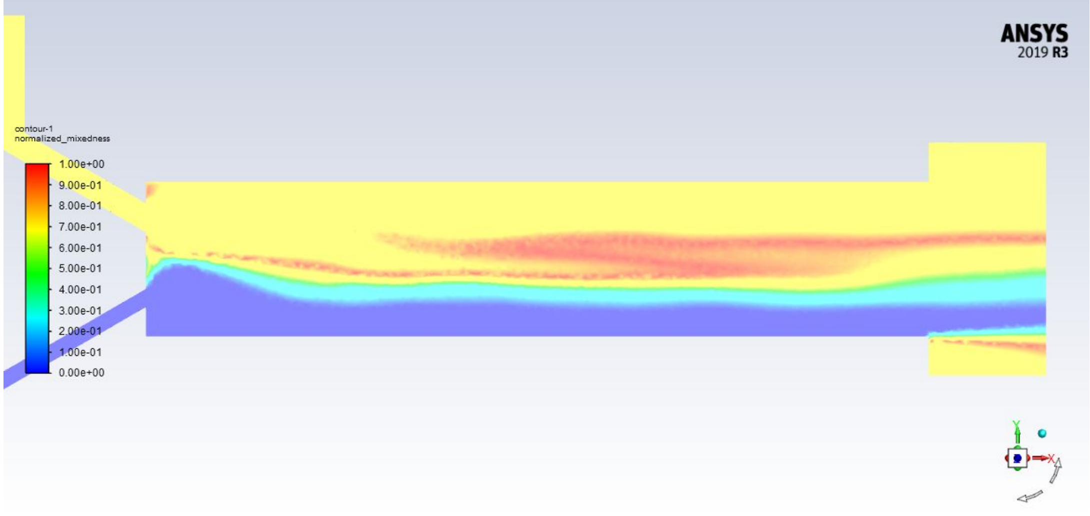

Figure B.4: Injector center plane contours of ξ for 25.4 mm RDRE 5-mm-gap configuration, run 192.

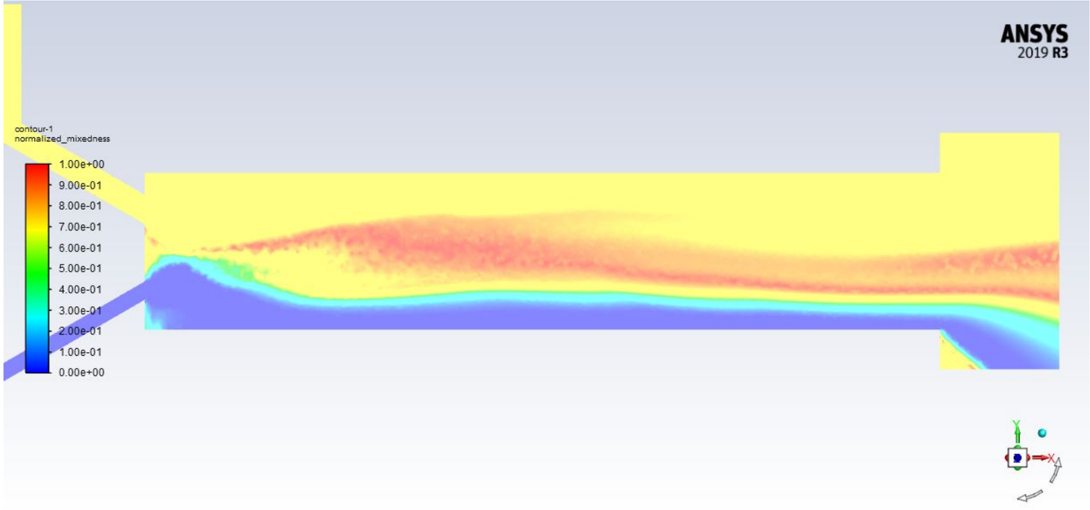

Figure B.5: Injector center plane contours of ξ for 25.4 mm RDRE 5-mm-gap configuration, run 234.

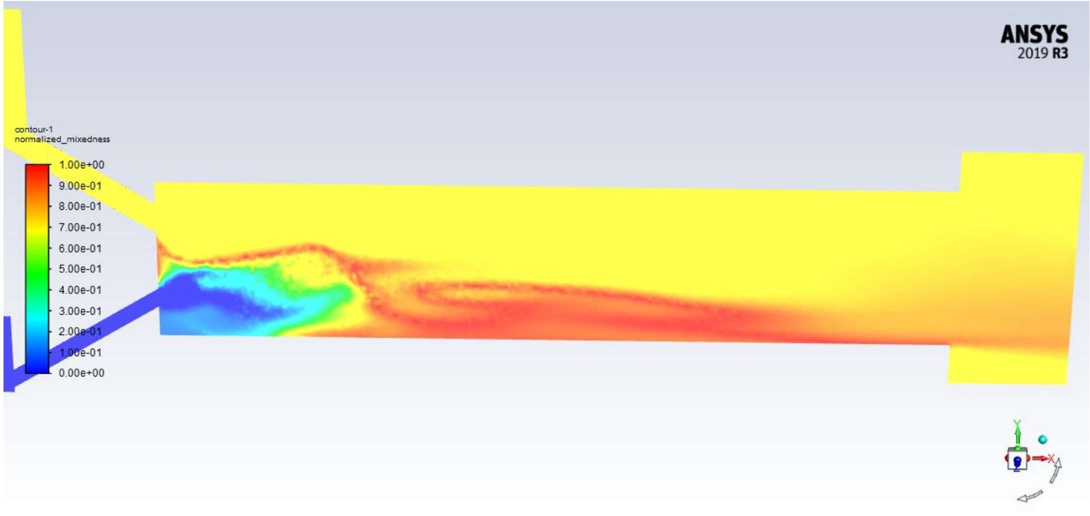

Figure B.6: Injector center plane contours of ξ for 25.4 mm RDRE 5-mm-gap configuration, run 408.

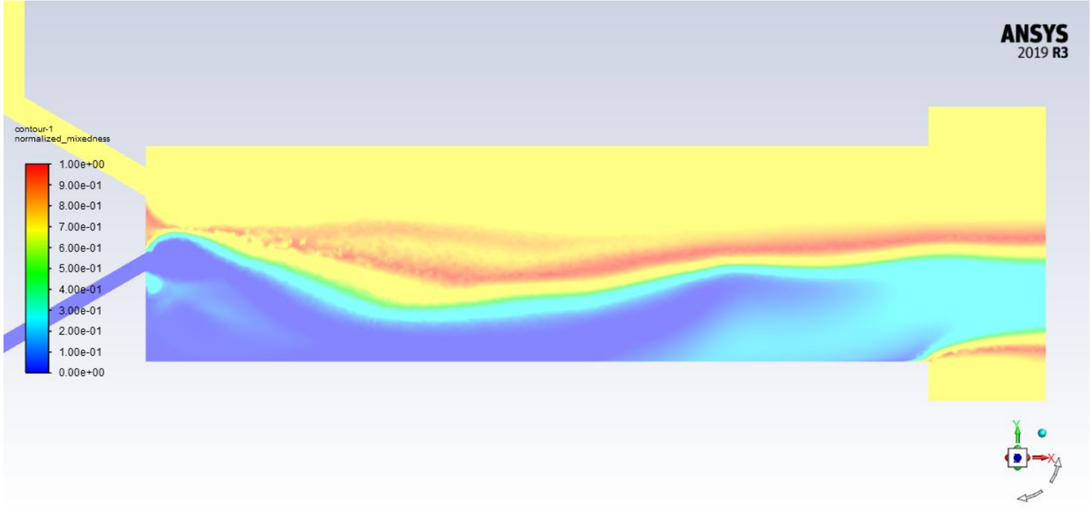

Figure B.7: Injector center plane contours of ξ for 25.4 mm RDRE 7-mm-gap configuration, run 337.

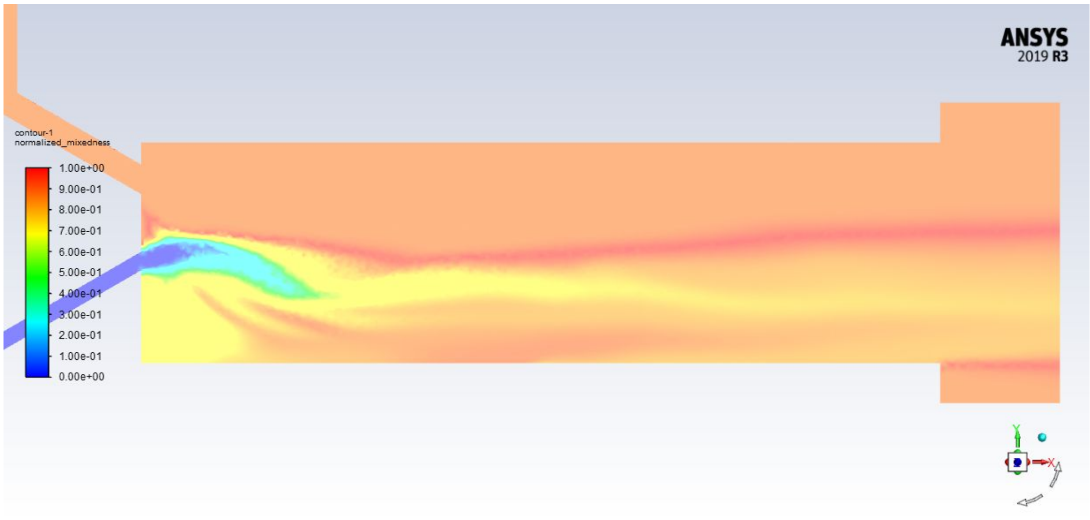

Figure B.8: Injector center plane contours of ξ for 25.4 mm RDRE 7-mm-gap configuration, run 338.

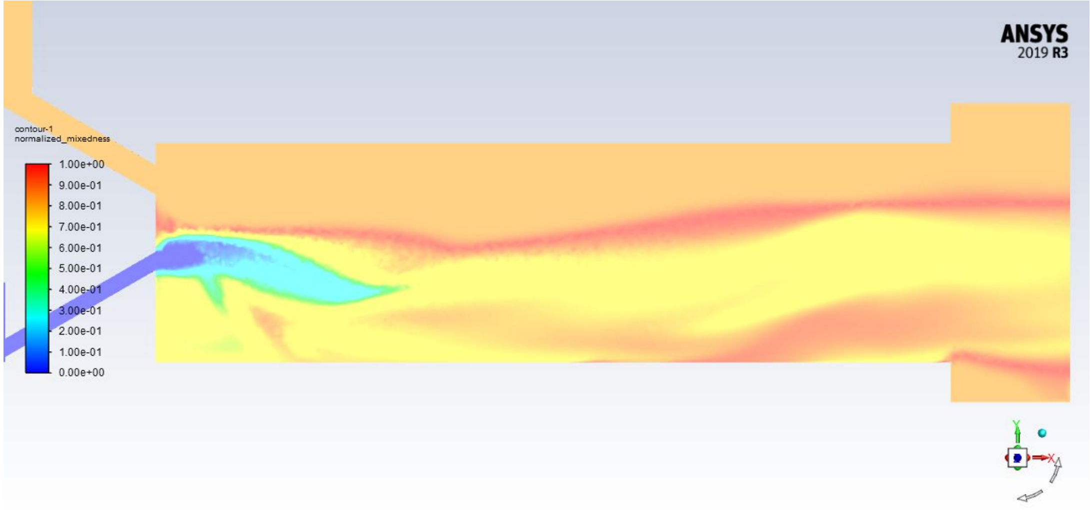

Figure B.9: Injector center plane contours of ξ for 25.4 mm RDRE 7-mm-gap configuration, run 342.

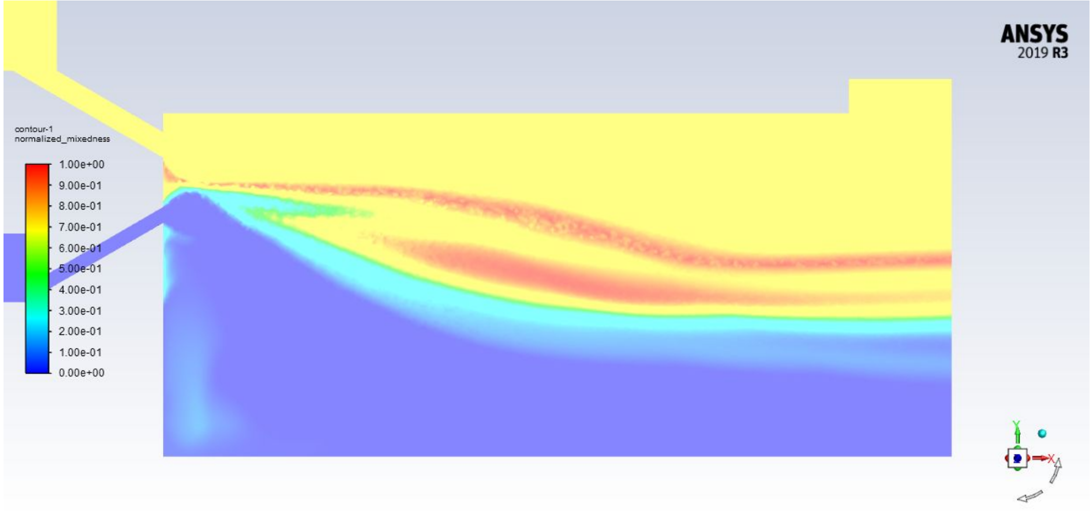

Figure B.10: Injector center plane contours of ξ for 25.4 mm RDRE coreless configuration, run 69.

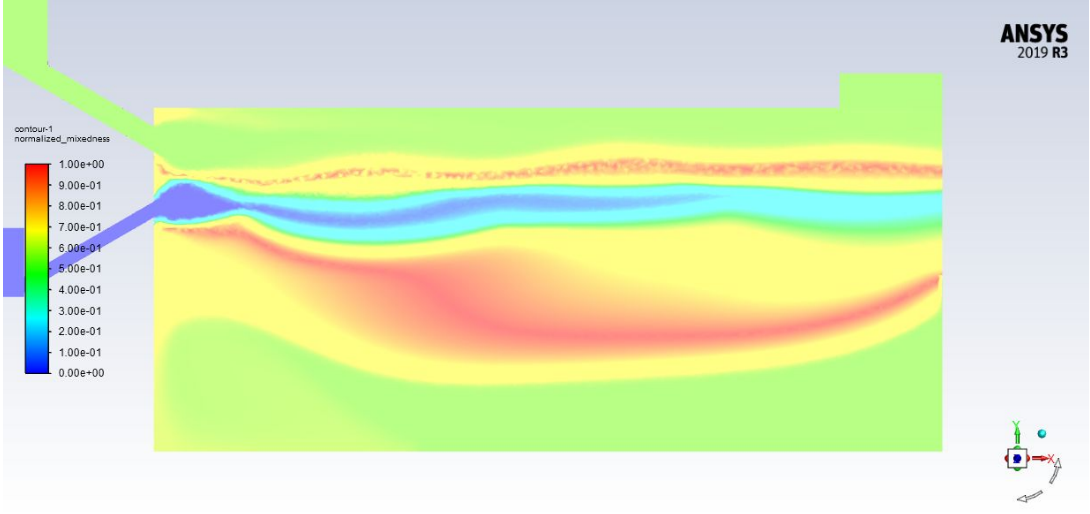

Figure B.11: Injector center plane contours of ξ for 25.4 mm RDRE coreless configuration, run 89.

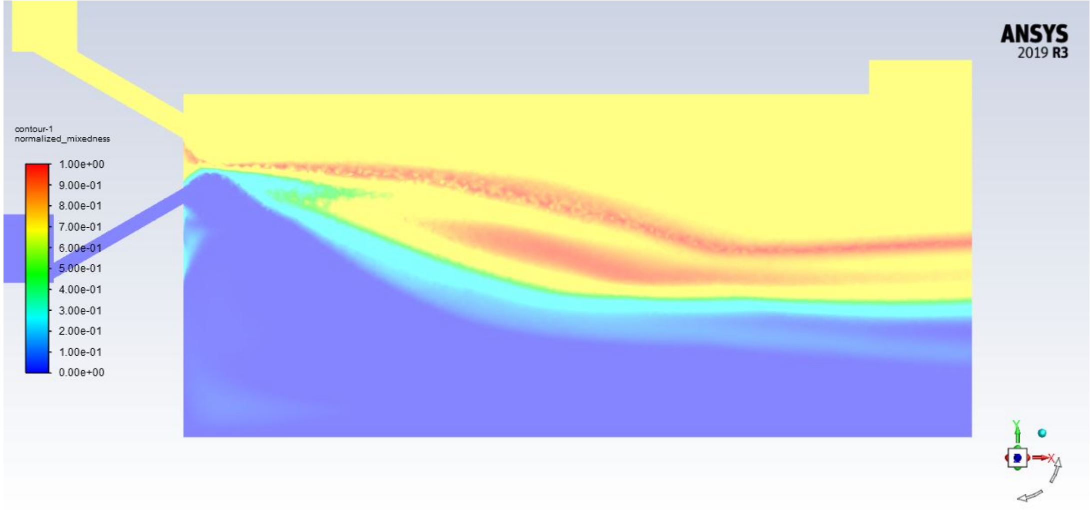

Figure B.12: Injector center plane contours of ξ for 25.4 mm RDRE coreless configuration, run 93.

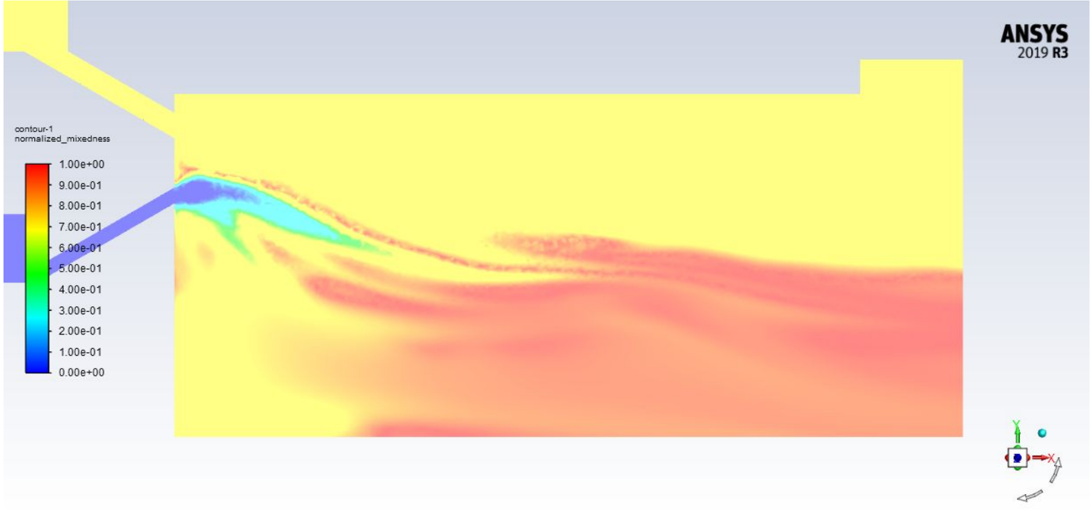

Figure B.13: Injector center plane contours of ξ for 25.4 mm RDRE coreless configuration, run 129.